## Anisotropic Proton Conductivity Arising from Hydrogen-Bond Patterns in Anhydrous Organic Single Crystals

### Mori Group

Proton conduction is a fundamentally important phenomenon not only in living systems but also in solid materials, such as fuel cells. Especially, the development of high proton conducting materials and the elucidation of the conducting mechanism are one of pivotal issues in this research field. Recently, organic acid-base salts have attracted increasing attention as a promising candidate of anhydrous proton conductors, which can be utilized as electrolyte of fuel cell above 100 ºC. In this study, we have successfully disclosed the relationship between proton conductivity and hydrogen-bond (H-bond) interactions in such kinds of organic salts, composed of dicarboxylic acid and imidazole [1].

We have grown high-quality single crystals of imidazolium succinate (Im-Suc) or glutarate (Im-Glu) by evaporation method in dehydrated methanol and dehydrated acetonitrile with a typical size of $0.5 \times 0.7 \times 1.0$ mm$^3$ (Im-Suc). As shown in Fig. 1, the crystal is composed of two-dimensional (2D) sheet structures, in which the imidazolium cations (Im) and succinate anions (Suc) are connected with hydrogen bonds (H-bonds) [2]. Two N–H moieties of the Im molecule are connected to carbonyl oxygen atoms of the Suc molecule with $d_{NO}$ of 2.72 Å (red dashed lines) and 2.87 Å (brown dashed lines) and also form short contacts with the adjacent oxygen atoms of the Suc molecule with $d_{NO} \sim 3.05$, 3.15 Å (blue dashed lines), like bifurcated H-bonds. In addition, a C-H···O short contact (gray dashed lines, $d_{CO} \sim 3.08$ Å) is observed between the Im and Suc molecules. Furthermore, there is an O-H···O H-bond between the Suc molecules (green dashed lines, $d_{OO} \sim 2.49$ Å). On the other hand, although the shortest C···C distance (3.39 Å) between the networks is less than the sum of van der Waals radii (3.40 Å), no effective H-bonds are found between these 2D networks (Fig. 1). The shortest N···O distances between the networks are 3.50 and 3.56 Å which are much longer than the sum of van der Waals (vdW) radii of N and O atoms (3.07 Å).

The relationship between the crystal shape and crystallographic axes was determined by X-ray diffraction measurements, where the [1 0 0] and [1 4 –9] directions are within the 2D network and the [0 1 1] is perpendicular to the 2D network (Fig. 1). Therefore, by measuring and comparing the proton conductivity in these three directions, we have revealed the effects of the H-bonding interactions and molecular arrangement on the proton conduction. By the measurement of ac proton conductivity, the complex impedance planes (Cole-Cole plots) gave almost perfect semicircle profiles at each temperature, which means that a single Debye-type relaxation occurs in our single-crystal

measurements and thus the obtained conductivity is the intrinsic proton conductivity without contributions from the grain boundaries. Then, we compare the proton conducting properties in these three directions (Fig. 1). First, the proton conductivity σ in the directions parallel to the H-bonding network (σ $_{[1\ 0\ 0]}$ and σ $_{[1\ 4\ –9]}$) and that in the direction perpendicular to the network (σ $_{[0\ 1\ 1]}$) are compared. At around 115 °C, the former two directions (σ $_{[1\ 0\ 0]}$ = 4.94 $\times 10^{-7}$ S cm$^{-1}$ and σ $_{[1\ 4\ –9]}$ = 1.27 $\times 10^{-7}$ S cm$^{-1}$) provide almost two orders higher conductivity than the latter one (σ $_{[1\ 0\ 0]}$ = 3.55 $\times 10^{-9}$ S cm$^{-1}$). This large difference is maintained in the present temperature range, indicating that the proton conduction occurs more readily in the H-bonding network than in its perpendicular direction.

Next, σ in the two directions parallel to the H-bonding network (σ $_{[1\ 0\ 0]}$ and σ $_{[1\ 4\ –9]}$) are compared. At 115 °C, the [1 0 0] direction has about four times higher σ (4.94 $\times 10^{-7}$ S cm$^{-1}$) than the [1 4 –9] direction (1.27 $\times 10^{-7}$ S cm$^{-1}$) and this trend is unchanged in this temperature region. The difference of σ between these two directions (about four times) is much smaller than that between the parallel and perpendicular directions (two orders) shown above. However, this small difference is significant in connection with anisotropy of the proton conduction in the 2D H-bonding network, especially in terms of the intermolecular interactions and molecular arrangement.

Moreover. in order to gain further insight into this relationship between the difference in $\Delta pK_a$ and the difference in the proton conductivity, we compare the present results with those of the analogues. The 1:1 co-crystals of benzimidazole, an imidazole derivative with $pK_{aH}$ = 5.49, and dicarboxylic acid are a similar type of H-bonded proton
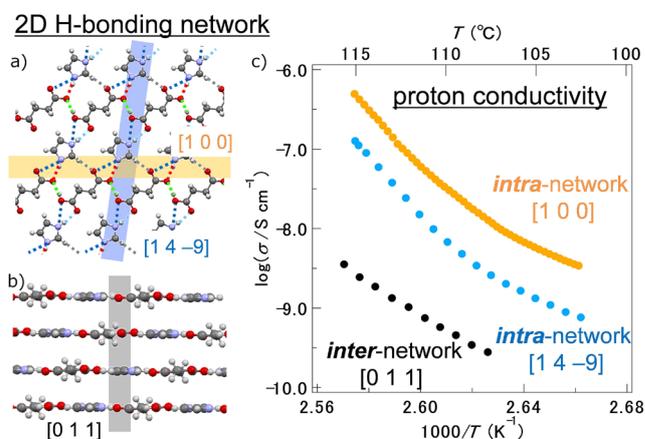


Fig. 1. a) Intra- and b) inter-2D-hydrogen (H)-bonded network [2], and c) anisotropic proton conduction along the [1 0 0], [1 4 –9], and [0 1 1] directions, respectively [1] for an anhydrous proton conductor, imidazolium succinate (Im-Suc). The proton conductivity in intra-network is by two-orders higher than that in inter-network. Moreover, the anisotropic proton conduction in intra-network demonstrates the importance of H-bonded molecular arrangement.

conductors, showing $\sigma$ = ~$10^{-5}$ S cm$^{-1}$ in the glutaric acid (pK$_{a1}$ = 4.34) salt and ~$10^{-4}$ S cm$^{-1}$ in the sebacic acid (pK$_{a1}$ = 4.72) salt in the compressed pellet state at around 77 °C. This result indicates that the latter salt with a smaller $\Delta$pK$_a$ of 0.77 (= 5.49 – 4.72) shows a higher proton conductivity than the former salt with a $\Delta$pK$_a$ of 1.15 (= 5.49 – 4.34). This trend is similar to that in the present imidazole systems, suggesting that the proton conductivity significantly increases with decreasing $\Delta$pK$_a$. However, the degree of the conductivity increase seems to be somewhat different in the benzimidazole and imidazole systems. Namely, the proton conductivity of the former system is increased one order of magnitude by the $\Delta$pK$_a$ difference of 0.38 (= 1.15 – 0.77), whereas that of the latter is increased 2–3 orders of magnitude by the $\Delta$pK$_a$ difference of 0.15 (= 2.76 – 2.61) as described before. Thus, simply stated, the proton conductivity of the present imidazole system is more sensitive to the pK$_a$ change than that of the benzimidazole system. This difference of the pK$_a$ effect on the proton conductivity probably originates from the difference in the molecular structure of imidazole and benzimidazole. Although these two systems have a similar overall crystal structure, the molecular structure difference would modulate the details, such as the intermolecular distances, H-bonding manners, and molecular arrangements, which result in the above-described difference in the pK$_a$ effect.

In conclusion, we have revealed the "intrinsic" proton conductivity without grain boundary contributions in acid-base type anhydrous organic single co-crystals, imidazolium succinate (Im-Suc) and imidazolium glutarate (Im-Glu), with a 2D H-bonding network. The obtained conductivities are 1~5 × $10^{-7}$ S cm$^{-1}$ (Im-Suc) and 2 × $10^{-6}$ S cm$^{-1}$ (Im-Glu) within the 2D H-bonding network, which are much higher than those in the perpendicular direction to the 2D network [4 × $10^{-9}$ S cm$^{-1}$ (Im-Suc) and 6 × $10^{-8}$ S cm$^{-1}$ (Im-Glu)]. These results demonstrate that the H-bonds significantly promote proton conduction in this kind of anhydrous materials. Furthermore, we have shown that this proton conduction is 1) more significant in the H-bonds between the acid and base molecules than in those between the acid and its conjugate base and is 2) enhanced by decreasing the difference of pK$_a$ between the H-bonded acid and base molecules. In addition, the present results offer the possibility that the molecular motions of imidazole play a crucial role in the proton conduction not only in the 2D H-bond network but also between the networks. The details about the inter-network proton conduction and also the non-Arrhenius-type profile of proton conductivity in the H-bond network are currently under investigation in terms of the molecular dynamics by using solid-state NMR and IR spectroscopies, high-temperature X-ray analysis, and theoretical calculations.

**References**
[1] Y. Sunairi, A. Ueda, J. Yoshida, K. Suzuki, and H. Mori, J. Phys. Chem. C, in press.
[2] J. C. MacDonald, P. C. Dorrestein, and M. M. Pilley, Cryst. Growth Des. **1**, 29 (2001).

**Authors**
Y. Sunairi, A. Ueda, J. Yoshida, K. Suzuki, and H. Mori

# Search for Topological States in an Organic Dirac Semimetal

## Osada Group

A layered organic conductor, $\alpha$-(BEDT-TTF)$_2$I$_3$, has been known as a two-dimensional (2D) gapless Dirac fermion system, namely, Dirac semimetal, with a pair of spin-degenerated Dirac cones. Generally, the Dirac semimetal is a starting point to obtain various topological insulating phases. In graphene, for example, Haldane showed that the Chern insulator (quantum anomalous Hall insulator) appears by attaching the alternating flux pattern breaking time reversal symmetry (TRS) [1]. On the other hand, Kane and Mele showed that the Z$_2$ topological insulator (quantum spin Hall insulator) appears by introducing the spin-orbit interaction (SOI) [2]. We have experimentally and theoretically explored the topological phases starting from the organic Dirac semimetal.

At ambient pressure, $\alpha$-(BEDT-TTF)$_2$I$_3$ undergoes a metal-insulator transition into an insulating phase due to the charge order (CO) at $T_c$=135K. This CO phase is suppressed by applying pressure, and it perfectly vanishes at about $P_c$~1.25GPa, as illustrated schematically in the inset of Fig. 1(a). Figure 1(a) shows the temperature dependence of in-plane resistance measured at several pressures. In the weak CO state around $P_c$, the resistance shows increase due to CO below $T_c$~50K, but the insulator-like increase turns to metal-like decrease at lower temperatures as shown by the red dashed circle. In addition, in the Dirac semimetal state above $P_c$, the resistance exhibits the insulator-like increase at low temperatures below 10K as indicated by the blue dashed circle. These behaviors have never been explained.

As their mechanisms, we propose the emergence of topological states in this organic system. First, we discuss the possible Chern insulator state in the weak CO state [3]. In the vicinity of CO transition, the NMR measurement by Kanoda's group clarified that not only the charge density but also spin density are modulated breaking TRS, as indicated by the clouds in Fig. 2(a). We assume a pattern of site potential and staggered magnetic flux on the $\alpha$-(BEDT-TTF)$_2$I$_3$ lattice so as to reproduce the observed potential and magnetic modulations (Fig. 2(a)). We shows that the system becomes a Chern insulator, where gaps open at two Dirac points, under large enough magnetic modulation, and one chiral edge state appears in the gap along each crystal edge (Fig. 2(a)). This is an organic analogue of the Haldane model. The conduction through these edge states explains
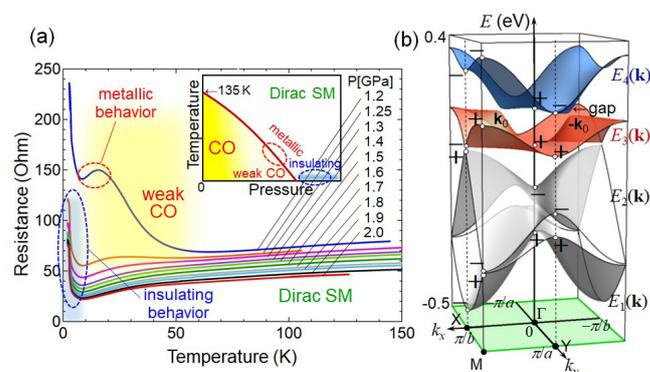


Fig. 1. (a) Temperature dependence of resistance in $\alpha$-(BEDT-TTF)$_2$I$_3$ at several pressures. (b) Band dispersion of $\alpha$-(BEDT-TTF)$_2$I$_3$. The symbols, "+" and "−", indicate parity at the time reversal invariant wave numbers.
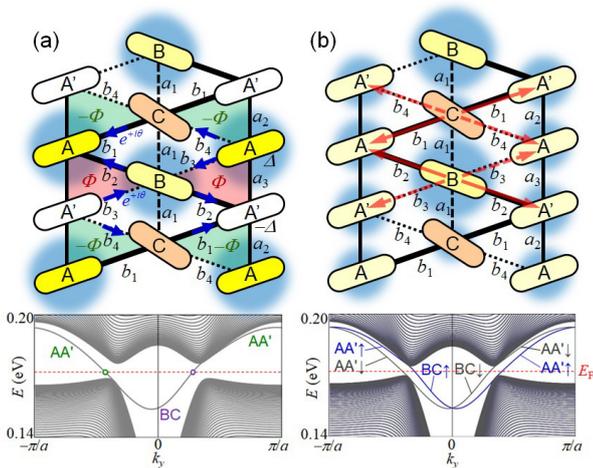
Fig. 2. (a) Flux configuration in the organic Haldane model. The lower panel shows the chiral edge state in the energy spectrum of the nanoribbon. (b) Inter-chain hopping with SOI in the organic Kane-Mele model. The lower panel shows the helical edge state in the energy spectrum of the nanoribbon.

the anomalous metallic behavior of resistance observed in the weak CO state.

Next, we discuss that the $Z_2$ topological insulator state with small gaps emerges in the Dirac semimetal state under finite SOI [4]. Using first principles calculations, Valenti *et al.* discussed that SOI in BEDT-TTF compounds could reach 1~2 meV, and finite SOI opens small gaps at Dirac points causing insulating behavior at low temperatures (Fig. 1(b)). We assume a pattern of inter-chain hopping accompanied by SOI on $\alpha$-(BEDT-TTF)$_2$I$_3$ lattice reflecting the charge disproportionation indicated by the clouds in Fig. 2(b). We demonstrate that gaps open at Dirac points causing resistance increase, and one helical edge state, which is characteristic to the topological insulator, appears in the gap along each crystal edge. This is an organic analogues of the Kane-Mele model. In addition, we generally discuss that a topological insulator appears under finite SOI as long as SOI does not cause any band inversion, based on the Fu-Kane parity product theory (Fig. 1(b)) [5]

References
[1] F. D. M. Haldane, Phys. Rev. Lett. **61**, 2015 (1988).
[2] C. L. Kane and E. J. Mele, Phys. Rev. Lett. **95**, 226801 (2005).
[3] T. Osada, J. Phys. Soc. Jpn. **86**, 123702 (2017).
[4] T. Osada, arXiv: 1804.09420.
[5] L. Fu and C. L. Kane, Phys. Rev. B **76**, 045302 (2007).

Authors
T. Osada, A. Mori, K. Yoshimura, M. Sato, T. Taen, and K. Uchida

# Thermal Hall Effect of Phonons

## Yamashita and Nakatsuji Groups

Hall measurements are fundamental probes for studying the physical properties of metals. Recently, Hall measurements in insulators, which are observed as *thermal* Hall effects (THEs), are being recognized as a new probe to study the elementary excitations in insulators. Since there is no charged heat carries in insulators, a THE in an insulator is not originated from the Lorentz force, but from intrinsic (e.g. Berry phase effect) or extrinsic (e.g. skew scatterings) mechanisms as the anomalous Hall effect. In fact, a THE of magnons has been observed in ferromagnetic insulators

below the Curie temperature [1], which has been understood in terms of the Berry phase effect [2, 3]. A THE of paramagnetic spins has also been reported in the spin-liquid phase of a kagomé antiferromagnet [4].

In spite of these recent studies of spin THEs, a phononic THE has remained elusive. A phonon THE was actually reported at 2005 in Tb$_3$Ga$_5$O$_{12}$ (TbGG) [5] prior to the observations of the spin THEs [1, 4]. However, the measurement of the phonon THE in TbGG was done only at ~5 K, disabling to find the temperature dependence of the thermal Hall conductivity ($\kappa_{xy}$). To find the theoretical model describing the phonon THE, it is indispensable to measure $\kappa_{xy}$ in a wide temperature range and to compare the temperature dependence with the theoretical predictions. Furthermore, because TbGG is paramagnetic at ~5 K, it is impossible to exclude a spin THE.

To this end, we performed thermal Hall measurements in the spin-liquid candidate Ba$_3$CuSb$_2$O$_9$ (BCSO) [6]. BCSO is a perovskite-type insulator, in which the spins of Cu2$^+$ ions form a honeycomb structure. NMR measurements show that a spin gap opens below ~50 K, enabling us to detect a phono THE without a spin THE.

Our main result is to find a distinct thermal Hall signal in a wide temperature range of 2-60 K, revealing that the phonon THE in BCSO shows $|\kappa_{xy}| \propto T^2$. As shown in Fig. 1, $\kappa_{xy}$ is negative in the entire temperature range measured, shows a peak around 50 K, and decreases at lower temperatures. A log-log plot of $|\kappa_{xy}|$ (inset of Fig. 1) shows that $|\kappa_{xy}| \propto T^2$ at low temperature. We conclude that the THE comes from phonons because a spin THE is supposed to show an activated temperature dependence owing to the spin gap formed below 50 K.

What is the mechanism of the phonon THE in BCSO? In TbGG, phonon scatterings by excess Tb$^{3+}$ ions have been pointed out as a possible mechanism of the phonon THE [8]. In BCSO, we also find the longitudinal thermal conductivity is strongly suppressed by a random structure of Cu$^{2+}$-Sb$^{5+}$ dumbbells. Therefore, this strong scattering effects on phonons in BCSO can be related to the phonon THE as that in TbGG. However, the $T^2$ dependence of $\kappa_{xy}$ has not been successfully reproduced by theories, which may be owing to the difference in scattering effects on phonons by the 4$f$ Tb$^{3+}$ ions with a large quadrupole moment and those by the 3$d$ Cu$^{2+}$ ions. We believe that our finding of $|\kappa_{xy}| \propto T^2$ leads to further theoretical and experimental studies to clarify the mechanism of phonon THEs in insulators.
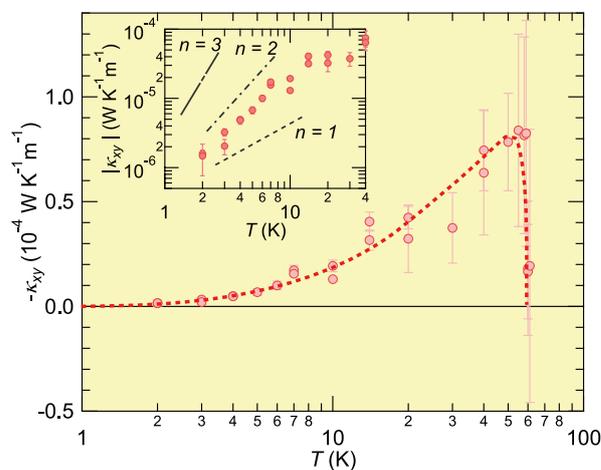


Fig. 1. The temperature dependence of thermal Hall conductivity ($\kappa_{xy}$). The dashed line is a guide for the eyes. The inset shows $|\kappa_{xy}|$ in log-log scale. The solid lines show slopes for $|\kappa_{xy}| \propto T^n$ ($n = 1, 2, 3$).

**References**
[1] Y. Onose *et al.*, Science **329**, 297 (2010).
[2] H. Katsura, N. Nagaosa, and P. A. Lee, Phys. Rev. Lett. **104**, 066403 (2010).
[3] R. Matsumoto, R. Shindou, and S. Murakami, Phys. Rev. B **89**, 054420 (2014).
[4] D. Watanabe *et al.*, Proc. Natl. Acad. Sci. USA **113**, 8653 (2016).
[5] C. Strohm, G. L. J. A. Rikken, and P. Wyder, Phys. Rev. Lett. **95**, 155901 (2005).
[6] S. Nakatsuji *et al.*, Science **336**, 559 (2012).
[7] K. Sugii, M. Shimozawa, D. Watanabe, Y. Suzuki, M. Halim, M. Kimata, Y. Matsumoto, S. Nakatsuji, and M. Yamashita, Phys. Rev. Lett. **118**, 145902 (2017).
[8] M. Mori *et al.*, Phys. Rev. Lett. **113**, 265901 (2014).

**Authors**
K. Sugii, M. Shimozawa, D. Watanabe, Y. Suzuki, M. Halim, M. Kimata, Y. Matsumoto, S. Nakatsuji, and M. Yamashita

# Quantum-Disordered State of Magnetic and Electric Dipoles in a Hydrogen-Bonded Organic Mott System

## Yamashita and Mori Groups

Strongly enhanced quantum fluctuations often lead to a rich variety of quantum-disordered states. A representative case is liquid helium, where zero-point vibrations of the helium atoms prevent its solidification at low temperatures. A similar behavior is found for the internal degrees of freedom in electrons. Among the most prominent is a quantum spin liquid (QSL), in which highly correlated localized spins fluctuate even at absolute zero. Recently, a coupling of spins with other degrees of freedom has been proposed as an innovative approach to generate even more fascinating QSLs, but such an idea is limited to the internal degrees of freedom in electrons.

The hydrogen-bonded organic Mott insulator $\kappa$-H$_3$(Cat-EDT-TTF)$_2$ (hereafter abbreviated as H-Cat) [1-3] synthesized by Mori group in ISSP shows considerable promise as a new type of QSLs, where H$_2$Cat-EDT-TTF is catechol-fused ethylenedithiotetrathiafulvalene. This compound has been reported to exhibit a two-dimensional (2D) QSL state; however, in contrast to other 2D organic QSL materials, the 2D $\pi$-electron layers of H-Cat are connected by hydrogen bonds, not separated by non-magnetic insulating layers. From the previous theoretical works [4,5], zero-point motion associated with this hydrogen atoms (termed "proton fluctuations") is believed to be strongly enhanced, leading to the realization of a QSL state through strong coupling between the hydrogen bonds and the $\pi$-electrons. However, it has not been established whether such strong quantum proton fluctuations are indeed present in H-Cat, and if so, how the quantum fluctuations affect the QSL state.

Here we demonstrate, by using a combination of dielectric permittivity and thermal conductivity measurements, that the quantum proton fluctuations in H-Cat provide a quantum-disordered state of magnetic and electric dipoles through the coupling between $\pi$-electrons and hydrogen atoms [6]. First of all, we focus on proton dynamics in H-Cat. As shown in Fig. 1, the dielectric constant $\varepsilon_r$ $(T)$ of H-Cat steeply increases with decreasing temperature and then saturates below 2 K. The temperature dependence of $\varepsilon_r$ $(T)$ for H-Cat is a typical dielectric behavior in quantum paraelectric (QPE) materials such as SrTiO$_3$, in which long-range electric order is suppressed by strong quantum fluctuations. From the fitting result by Barrett formula describing the QPE state, we

have found the presence of an antiferroelectric (AFE) interaction in H-Cat, which is consistent with the AFE configuration resulting from a hydrogen-bond order in the deuterated analog of H-Cat, $\kappa$-D$_3$(Cat-EDT-TTF)$_2$ (denoted as D-Cat) [3]. Thus, the observed quantum paraelectricity in H-Cat clearly shows the presence of strong quantum fluctuations that suppress the hydrogen-bond order as observed in D-Cat, that is, the persistence of enhanced proton fluctuations down to low temperatures.

We next examine how the proton dynamics in the QPE state affects the nature of the QSL state in H-Cat. For this purpose, in Figure 1, we plot the temperature dependence of the thermal conductivity divided by temperature $\kappa/T$ (this work) and the magnetic susceptibility $\chi$ [2] for H-Cat, together with the above-mentioned $\varepsilon_r$. Below 2 K, the thermal conductivity increases upon entering the QPE state, where $\varepsilon_r$ saturates. The characteristic temperature coincides with the temperature at which the susceptibility becomes constant; this occurs when the spin correlation develops in the QSL state. The coincidence of the QPE and QSL states is surprising and strongly suggests that the development of the quantum proton fluctuations triggers the emergence of the QSL. We now theoretically analyze the effects of proton dynamics on the QSL state. According to our model that captures the essence of H-Cat system [7], low-energy proton fluctuations (~1 meV) modulate the amplitude of the electron transfers and the energy levels of the molecular orbitals. These effects may induce a dynamical modulation of exchange coupling energy $J$ as well as a reduction of the on-site Coulomb repulsion $U$ due to the bi-polaron effect. As a result, the magnetic long-range order would be suppressed by proton dynamics of H-Cat, inducing a QSL.

In conclusion, we have successfully discovered a quantum-disordered state of magnetic and electric dipoles in a hydrogen-bonded organic Mott system, H-Cat. Importantly, this system has 2D $\pi$-electron layers connected by hydrogen bonds, in contrast to the other organic QSL candidates with those separated by anion layers. This structural feature of H-Cat enables us to discover a new mechanism to stabilize the QSL state, where the electron and proton degrees of freedom are strongly coupled. Utilizing such a strong coupling between multiple degrees of freedom will advance our explorations of quantum phenomena such as orbital–spin liquids and electric–dipole liquids.
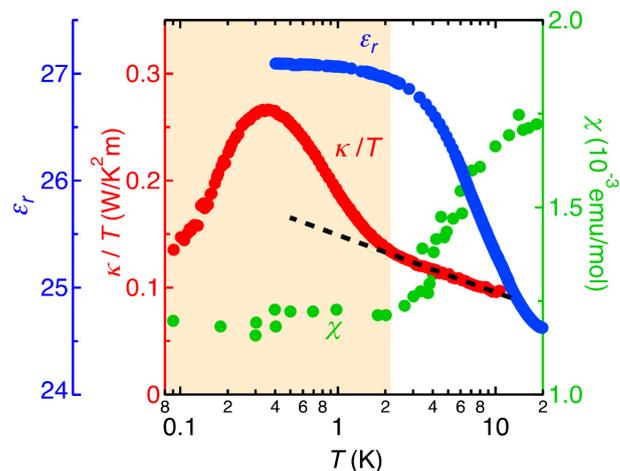


Fig. 1. A combination of the temperature dependences of the dielectric constant $\varepsilon_r$ (blue, left axis), the thermal conductivity divided by temperature $\kappa/T$ (red, left axis) and the magnetic susceptibility $\chi$ (green, right axis) for H-Cat. The values of $\chi$ are taken from ref. 2. The dashed line is an eye guide. The shaded region represents the QPE and QSL phases.

**References**
[1] T. Isono *et al.*, Nat. Commun. **4**, 1344 (2013).
[2] T. Isono *et al.*, Phys. Rev. Lett. **112**, 177201 (2014).
[3] A. Ueda *et al.*, J. Am. Chem. Soc. **136**, 12184 (2014).
[4] T. Tsumuraya, H. Seo, R. Kato and T. Miyazaki, Phys. Rev. B **92**, 035102 (2015).
[5] K. Yamamoto *et al.*, Phys. Chem. Chem. Phys. **18**, 29673(2016).
[6] M. Shimozawa *et al.*, Nat. Commun. **8**, 1821 (2017).
[7] M. Naka and S. Ishihara, arXiv:1801.04661.

**Authors**
M. Shimozawa, K. Hashimoto[a], A. Ueda, Y. Suzuki, K. Sugii, S. Yamada, Y. Imai, R. Kobayashi[a], K. Itoh[a], S. Iguchi[a], M. Naka[b], S. Ishihara[b], H. Mori, T. Sasaki[a], and M. Yamashita
[a]Institute for Materials Research, Tohoku University
[b]Tohoku University

# Disguised Antiferromagnetic Order in a Two-Dimensional Quasicrystal

## Tsunetsugu Group

Quasicrystals are the alloys with a lattice structure that is not consistent with translation symmetry but its Fourier pattern $S(\boldsymbol{k})$ comprises a set of delta-function peaks like those in crystals. In most of quasicrystals, however, the structure factor has a rotation symmetry that is prohibited in crystals and also self-similarity $S(\lambda^{-n}\boldsymbol{k}) \sim \Lambda^{-n} S(\boldsymbol{k})$. It is expected that this unique lattice structure has a crucial effect on magnetic order driven by strong electron correlation, and we have explored this issue in the simplest quasicrystal, the Penrose lattice in two dimensions. The Penrose lattice has the five-fold rotation symmetry, characterized by the geometrical factor known as the golden ratio $\tau = 2\cos(\pi/5) = (\sqrt{5} + 1)/2$

To study an antiferromagnetic order in the Penrose lattice, we have employed the half-filled Hubbard model with sites on the vertices of rhombus units. When the Coulomb repulsion is switched off ($U = 0$), this model has a thermodynamically degenerate single-electron states called *confined states*; each of them is strictly confined in a finite region of the lattice [1]. Since their energy locates at the center of spectrum $E = 0$, they contribute to the formation of magnetic moments, upon switching on $U$.

Magnetic moments have nonvanishing amplitudes at most of sites, even in the limit of $U \rightarrow +0$; the site average of moment size is 81/2–25 $\tau \sim 0.05$. We know that they should exhibit an antiferromagnetic long-range order at zero
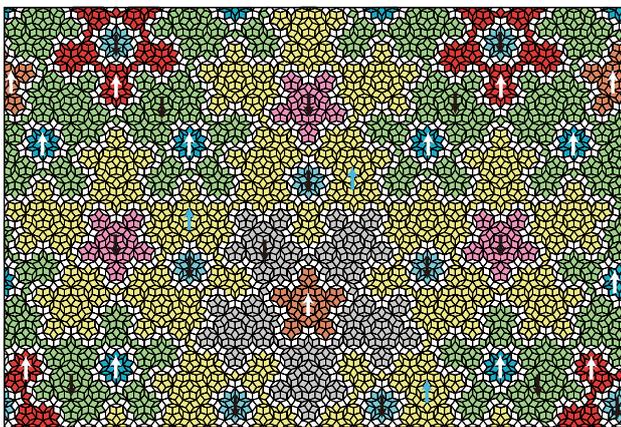


Fig. 1. Disguised antiferromagnetic order in the Penrose lattice. In each cluster, only one-sublattice sites have nonvanishing magnetic moments at $U$=+0, and they polarize in the same direction marked by arrow, whereas the moment size is zero everywhere in the other sublattice.

temperature, because the Penrose lattice is bipartite despite the lack of translation symmetry. A big surprise is that this antiferromagnetic order is disguised and the moments exhibit a very complicated fractal-like spatial pattern. The magnetic order is cluster antiferro; moments are polarized in the same direction in each cluster, and neighboring clusters polarize in the opposite directions [2]. The clusters have sizes ranging from 31 sites to infinity, and their densities follow a power-law scaling with their size. This is an intricate consequence of quasiperiodic lattice structure. With increasing $U$, the magnetizations of minority spin continuously evolve, and the magnetic order approaches a conventional Néel type with staggered magnetization. This crossover depends on local environment of each site, and it is also dominated by the quasiperiodic structure.

This study is performed by collaboration with Akihito Koga at Tokyo Institute of Technology.

**References**
[1] M. Arai, T. Tokihiro, T. Fujiwara, and M. Kohmoto, Phys. Rev. B **38**, 1621 (1988).
[2] A. Koga and H. Tsunetsugu, Phys. Rev. B **96**, 214402 (2017).

**Author**
H. Tsunetsugu

# Interaction Effect on Adiabatic Charge Pumping via a Single-Level Quantum Dot

## Kato Group

Charge transport from one reservoir to another reservoir induced by periodic operation on devices is called "charge pumping". Recent development of device fabrication and measurement technique has enabled us to realize charge pumping in nanoscale devices such as quantum dots (QDs). In particular, quasi-static pumping under slow parameter driving, i.e., "adiabatic" pumping is an important phenomenon because pumping charge depends only on a trajectory in the parameter space. Application of adiabatic pumping to, e.g., current standard and single electron injection has been discussed in a number of theoretical and experimental works [1].

For adiabatic pumping, we need to take a period of driving as larger than characteristic time scales of the system. Therefore, coherent transport in quantum dots strongly coupled with electronic leads, which have a short relaxation time, is suitable to fast adiabatic pumping. However, theoretical framework for charge pumping in QDs strongly mixed with leads has not been studied so far. In our previous paper [2], we calculated pumping charge within the first-
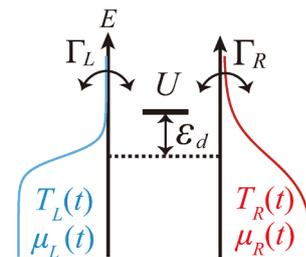


Fig. 1. Schematics of our model for adiabatic charge pumping due to driving of reservoir parameters (temperatures and electrochemical potentials). Here, $\varepsilon_d$ and $U$ are an energy level and a Coulomb interaction in a quantum dot, respectively. The dot-reservoir couplings are denoted by $\Gamma_L$ and $\Gamma_R$.

**(a) Electrochemical-potential driving**

$u = 0.5, 1, 2, 3, 4$

Pumped charge per a cycle

$\Gamma_L = \Gamma_R = \Gamma/2$

$u \equiv U/\Gamma$

$(\varepsilon_d - U/2) / \Gamma$

**(b) Temperature driving**

$u = 0.5, 1, 2, 3, 4$

Pumped charge per a cycle

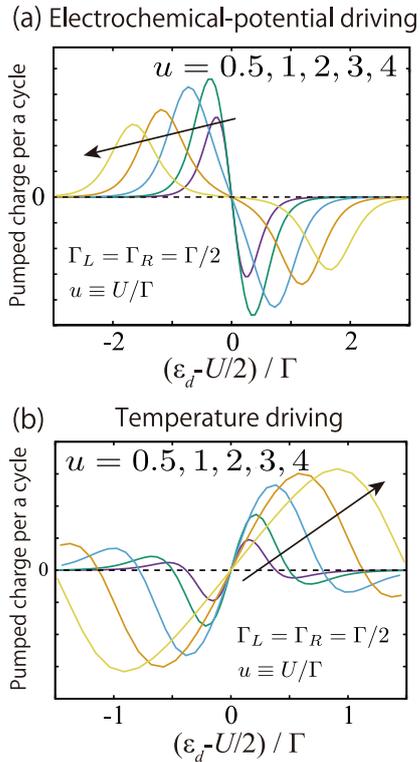$\Gamma_L = \Gamma_R = \Gamma/2$

$u \equiv U/\Gamma$

$(\varepsilon_d - U/2) / \Gamma$

Fig. 2. Pumped charge per one cycle obtained by the renormalized perturbation theory for (a) the electrochemical-potential driving case and (b) the temperature-driving case.

order perturbation theory with respect to Coulomb interaction. In the present study [3], we aimed to construct general formalism, which can treat arbitrary strength of Coulomb interaction beyond our previous work.

We considered adiabatic charge pumping via a single-level QD system induced by reservoir parameter driving in the coherent transport region (see Fig. 1). We formulated pumped charge for arbitrary Coulomb interaction by nonequilibrium Green's function method. To handle the time-dependent reservoir temperatures, we introduced a thermomechanical field, which describes temperature modulation via an energy rescaling of the reservoirs. We also employed the adiabatic approximation to obtain pumped charge under adiabatic operation.

We derived a general formula for the pumped charge in terms of the Berry connection. It is expressed by the two-particle Green's function of electrons in the QD. Our formalism covers the low-temperature strongly-correlated region, which cannot be treated in the previous theoretical methods. Based on our general formulism, we calculated the pumped charge by employing the renormalized perturbation theory (see Fig. 2). We showed that for both the electrochemical-potential-driven and the temperature-driven case, the pumping strength has a maximum and a minimum as a function of the QD energy level, and the position of the maximum (minimum) moves away from the particle-hole symmetric point as the Coulomb interaction increases. For the electrochemical-potential-driven case, the maximum value of the pumping strength is once enhanced, and then suppressed as the Coulomb interaction increases (see Fig. 2 (a)). On the other hand, for the temperature-driven case, the maximum value continues to increases as the Coulomb interaction increases (see Fig. 2 (b)). This difference was explained from the renormalized parameters consistently.

Our formalism states that adiabatic charge pumping can be evaluated by the two-particle Green's function of

the electrons in the QD, which is in principle calculated by numerical methods. It is an important future problem to compute the pumped charge without any approximation in the strong Coulomb interaction region. From the viewpoint of non-equilibrium thermodynamics, it is also a challenge to generalize the present formalism to heat pumping and work exchange and to discuss quantum effects on efficiency of small engines.

**References**
[1] J. P. Pekola *et al.*, Rev. Mod. Phys. **85**, 1421 (2013).
[2] M. Hasegawa and T. Kato, J. Phys. Soc. Jpn. **86**, 024710 (2017).
[3] M. Hasegawa and T. Kato, J. Phys. Soc. Jpn. **87**, 044709 (2018).

**Authors**
M. Hasegawa and T. Kato

# Crossover between Kondo States in Carbon Nanotube Quantum Dot Observed by an Ultrasensitive Noise Measurement

## Kato Group

We have realized the SU(2) and SU(4) Kondo many-body states in a carbon nanotube quantum dot made by the cutting-edge nanofabrication technology, and finely controlled a crossover phenomenon between the two Kondo states by applying magnetic fields. Our very accurate current noise measurement successfully elucidated that the local moment structure within the quantum dot can be adjusted to increase the quantum fluctuation of the Kondo state [1].

The Kondo effect is a typical quantum many-body phenomenon, where electrons gather around the moment of a localized electron and form a new state (Kondo state) together and quantum fluctuation of the angular moment of the electrons plays the essential role in formation of the Kondo state. The electrons confined in the carbon nanotube quantum dot hold not only spin but also additional degrees of freedom, namely, the direction of electron motion (see Fig. 1), which brings a variety to the Kondo state. However, it is not easy to distinguish the SU(2) and SU(4) Kondo states by power laws emerging in observed current as function of temperatures or applied bias-voltages, because both of the Kondo states are governed by the local Fermi liquid. The key idea of our work is to observe and analyze current noise. The Fano factor given by the ratio of the nonlinear current noise and the nonlinear current repre-



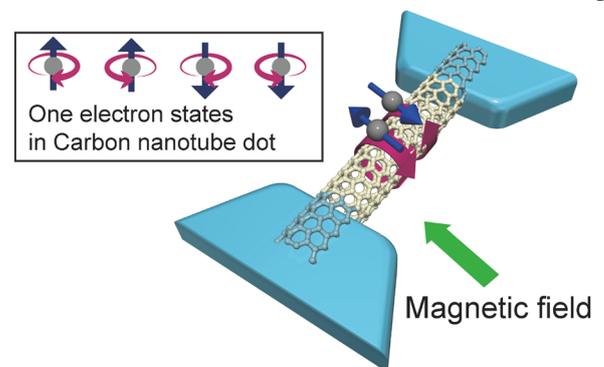One electron states in Carbon nanotube dot

Magnetic field

Fig. 1. Two aluminum electrodes (cyan) are attached to a carbon nanotube quantum dot (yellow). Electric current and its noise through them are investigated. Electrons confined in the carbon nanotube dot hold not only the spin degree freedom but also a degree of freedom due to the direction of electron motion (red arrows wrapped around the nanotube), which can bring a rich variety of the Kondo state.
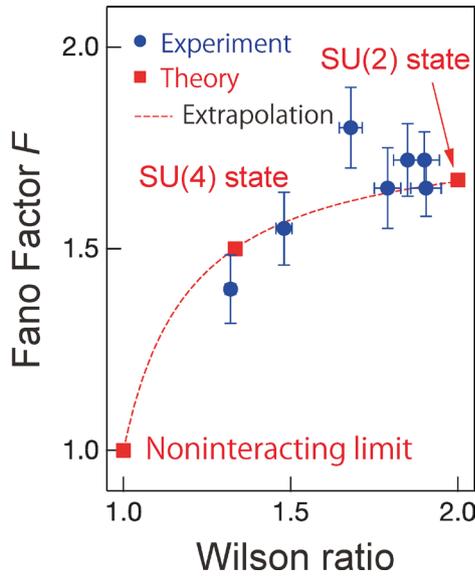
Fig. 2. Fano factor as a function of the Wilson ratio.

# In-Plane Spin Filtering in a Resonant Diode with Double Quantum Well

## Katsumoto Group

A quantum resonant diode is a device that filters the electron momentum perpendicular to the quantum well. Combined with the energy conservation, this restricts the electrons which can tunnel through the device into a circle on the Fermi surface in the source. The momentum selection may lead to spin selection due to spin-momentum locking via strong spin-orbit interaction (SOI). This can be achieved, for example, in a series connection of two quantum wells with opposite sign Rashba SOI coupling constants to each other [1]. However this device does not have practical meaning because Rashba-type SOI does not have in-plane anisotropy and without in-plane selection of momentum, the device does not work as a spin-filter. Now, if Dresselhaus-type SOI co-exists, the in-plane symmetry of the system lowers and the device can have bi-directional spin-filtering effect.

Here we have realized such a device of double quantum well with n-p-n type doping, which provides opposite sign Rashba SOI for the two quantum wells. The materials are zinc-blende InGaAs quantum wells and AlInAs barriers lattice matched to a (001) InP substrate. Hence the system has a Dresselhaus SOI lacking the inversion symmetry. On top of the resonant diode layers, an iron single crystal with body-centered cubic (bcc) lattice structure is deposited.

The left panel of Fig. 1 shows the differential resistance as a function of bias voltage in negative bias range. Negative resistances appear at two resonant energies as double dips reflecting the double well avoided crossing. Around the origin of the I-V characteristics, no trace of Fe magnetization appears in the in-plane field magnetoresistance. Just above $E_1$ resonance, hysteretic magnetoresistance (MR) shown in the right panel of Fig. 1 appears. The lineshape resembles to that of so called anisotropic magnetoresistance (AMR) suggesting that the lineshape itself has the same origin, that is the magnetic domain formation in the Fe layer. However, the amplitude in the resistance is far above the AMR in Fe.

The left panel of Fig. 2 shows the MR for the field down sweep in color plot versus the plane of field strength and directional angle from $[\bar{1}10]$. As shown in the polar plot at the right, the anisotropy apparently reflects the symmetry of the Dresselhaus SOI while the coercive force as observed in the width of MR, reflects the four-fold bcc symmetry of the Fe layer. All the observations indicate the resonant double
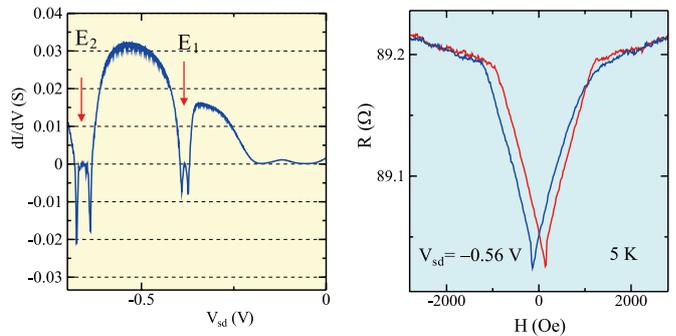
sents a strength of the local-Fermi-liquid interaction, which indicates a strength of quantum fluctuation of the Kondo ground state. The Fano factor also shows an intrinsic value corresponding to the local moment which causes the Kondo state.

Figure 2 shows the observed Fano factor $F$ as a function of the Wilson ratio $R$. In our experiment, the Wilson ratio is controlled by applied magnetic field. The values of the Wilson ratio corresponding to experimentally applied magnetic field are estimated by numerical renormalization calculation [2]. The Wilson ratio are varied from $R = 4/3$ at the zero magnetic field, where the SU(4) Kondo state is realized, to $R = 2$, the large magnetic field limit where the SU(2) Kondo state is realized. In Fig. 2, the Fano factor varies from $F = 1.4 \pm 0.1$ at the zero field to $F = 1.7 \pm 0.1$ at a large field. These observations well agree with $F = 3/2$ and $5/3$ theoretically predicted for the SU(2) and SU(4) Kondo states, respectively [3, 4].

In this research, we have experimentally demonstrated that the strength of quantum fluctuation depends on the type of Kondo states. Both the Kondo effect and quantum fluctuation are central issues in physics. Our result brings a deeper understanding of quantum many-body phenomena, and opens a new way to control quantum fluctuation and to explore new function of materials.

### Refernces
[1] M. Ferrier, T. Arakawa, T. Hata, R. Fujiwara, R. Delagrange, R. Deblock, Y. Teratani, R. Sakano, A. Oguri, and K. Kobayashi, Phys. Rev. Lett. **118**, 196803 (2017).
[2] Y. Teratani, R. Sakano, R. Fujiwara, T. Hata, T. Arakawa, M. Ferrier, K. Kobayashi, and A. Oguri, J. Phys. Soc. Jpn. **85**, 094718 (2016).
[3] R. Sakano, T. Fujii, and A. Oguri, Phys. Rev. B **83**, 075440 (2011).
[4] R. Sakano, A. Oguri, T. Kato, and S. Tarucha, Phys. Rev. B **83**, 241301(R) (2011).

### Authors
R. Sakano, M. Ferrier[a], T. Arakawa[b], T. Hata[c], K. Kobayashi[b], Y. Teratani[d], and A. Oguri[d]
[a]Université de Paris-Sud
[b]Osaka University
[c]Tokyo Institute of Technology
[d]Osaka City University

Fig. 1. Left: Differential resistance of an InGaAs double quantum well resonant diode as a function of source-drain negative bias voltage. $E_1$ and $E_2$ correspond to the resonant energy levels. Right: Hysteretic in-plane magnetoresistance appeared above the resonant level $E_1$. The field direction is along $[\bar{1}10]$. Blue and red lines correspond to down and up field sweeps respectively.
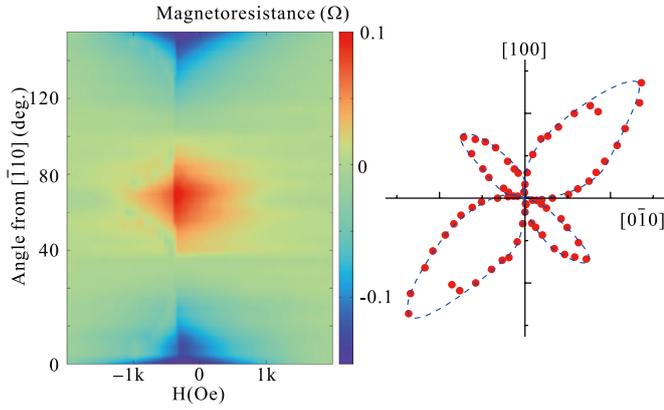
Fig. 2. Left: Color level plot of the magnetoresistance as a function of field strength and angle from [110]. The sign is reversed around [100] (45°) and [010] (90°). Right: Polar plot of magnetoresistance amplitude for the in-plane field direction.

well diode is working as an in-plane spin filter caused by the combined effect of Rashba and Dresselhaus SOIs.

**Reference**
[1] T. Koga, J. Nitta, H. Takayanagi, and S. Datta, Phys. Rev. Lett. **88**, 126601 (2002).

**Authors**
T. Nakamura, Y. Hashimoto, and S. Katsumoto

# Clear Variation of Spin Splitting by Changing Electron Distribution at Non-magnetic Metal/Bi$_2$O$_3$ Interfaces

## Otani Group

Edelstein effect, the spin-to-charge current interconversion at interfaces [1], has attracted much attention. An efficient interconversion at Cu/Bismuth oxide (Bi$_2$O$_3$) interface has been discovered [2, 3], which is attributed to a large Rashba splitting in the electronic state at the metal/oxide interface (see Fig. 1 (1)). However, the guiding principle of designing the metal/oxide interface with large Rashba splitting for the efficient conversion is missing. In this study, we report strong non-magnetic (NM) material dependence of spin splitting at NM/Bi$_2$O$_3$ interface and discuss the origin of the NM dependence with first-principles calculations.

We employed spin pumping technique to inject spin current into the NM/Bi$_2$O$_3$ (NM = Al, Cu, Ag, Au) interface. The injected spin current is converted to charge current by the inverse Edelstein effect (spin-to-charge conversion at the interface, see Fig. 1 (b)). We evaluated the conversion coefficient and the Rashba parameter $\alpha_R$ which determines the splitting in momentum between spin-up and spin-down electrons. The evaluated $\alpha_R$ are $-0.055$, $-0.25$, $+0.15$
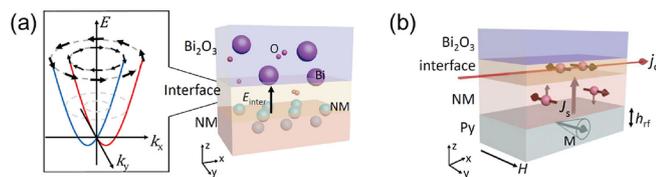


Fig. 1. (a) Rashba spin splitting at NM/Bi$_2$O$_3$ interface. (b) Schematic of spin-to-charge conversion at the NM/Bi$_2$O$_3$ interface. A spin current is injected from the Py layer into the NM/Bi$_2$O$_3$ interface, and then converted to the charge current via the inverse Edelstein effect.
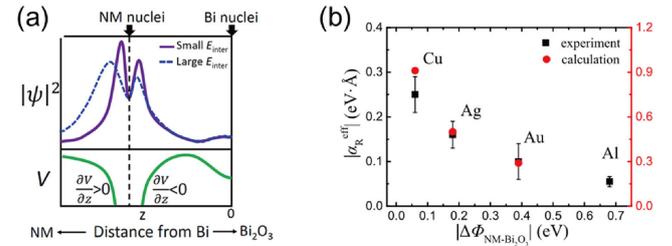


Fig. 2. (a) An asymmetry distribution of $|\Psi|^2$ generated by interfacial electric field. Purple line and blue line show the $|\Psi|^2$ under smaller and larger electric field, respectively. Green line show electrostatic potential $V$. (b) Absolute value of $\alpha_R$ estimated by the experiment and the calculation in different NM/Bi$_2$O$_3$ interfaces as a function of $|\Delta\Phi_{NM-Bi2O3}|$.

and $-0.09$ eV·Å for NM = Al, Cu, Ag and Au, respectively.

The Rashba parameter $\alpha_R$ can be described as,

$$\alpha_R = \frac{2}{c^2} \int \frac{\partial V}{\partial z} |\Psi|^2 \, dz, \qquad (1)$$

where $c$, $\partial V/\partial z$ and $|\Psi|^2$ are the speed of light, potential gradient and electron density distribution, respectively. Schematic illustration of $V$ and $|\Psi|^2$ at NM/Bi$_2$O$_3$ interfaces based on our ab-initio calculation is shown in Fig. 2 (a). $|\Psi|^2$ can be modulated by the out-of-plane electric field $E_{inter}$ at the interface. Note that $E_{inter}$ originates from work function difference $\Delta\Phi_{NM-Bi2O3}$ between NM and Bi$_2$O$_3$. The asymmetry feature of $|\Psi|^2$ which depends on $E_{inter}$ and $\Delta\Phi_{NM-Bi2O3}$ should be important for the magnitude and the sign of $\alpha_R$.

Figure. 2(b) shows $|\alpha_R|$ estimated by experiment and calculation in different NM/Bi$_2$O$_3$ as function of $|\Delta\Phi_{NM-Bi2O3}|$. $|\alpha_R|$ decreases as $|\Delta\Phi_{NM-Bi2O3}|$ increases and the trend of calculated $|\alpha_R|$ is in good agreement with the experiment. This trend can be explained as follows (see Fig. 2 (a)). $|\Psi|^2$ is strongly localized near NM nuclei when $E_{inter}$ is small, while $|\Psi|^2$ could be shifted from nuclei and delocalized when $E_{inter}$ is large. The steepest $\partial V/\partial z$ is located near NM nuclei. Thus, larger $E_{inter}$ (larger $|\Delta\Phi_{NM-Bi2O3}|$) gives smaller integral in Eq. (1). The opposite sign of $\alpha_R$ between Ag/Bi$_2$O$_3$ and other interfaces may be explained by different sign of $\Delta\Phi_{NM-Bi2O3}$ at Ag/Bi$_2$O$_3$ from others. Assuming that Ag/Bi$_2$O$_3$ and Cu/Bi$_2$O$_3$ interfaces have similar hybridization state, the opposite direction of $E_{inter}$ may shift the $|\Psi|^2$ to different side of NM or Bi$_2$O$_3$ and cause the sign change of the integral.

We found that the asymmetry feature of $|\Psi|^2$ which can be modulated by $\Delta\Phi_{NM-Bi2O3}$ results in strong NM dependence on $\alpha_R$. Our study suggests that control of interfacial electron distribution by changing the difference in work function across the interface may be an effective way to tune the magnitude and sign of Rashba splitting and the spin-to-charge current interconversion at interface.

**References**
[1] J. C. R. Sánchez *et al.,* Nat. Commun. **4**, 2944 (2013).
[2] S. Karube, K. Kondou, and Y. C. Otani, Appl. Phys. Express **9**, 033001(2016).
[3] J. Kim, Y. T. Chen, S. Karube, S. Takahashi, K. Kondou, G. Tatara, and Y. Otani, Phys. Rev. B **96**, 140409(R) (2017).

**Authors**
H. Isshiki and Y. Otani

# Modulation of Electron-Phonon Coupling in One-Dimensionally Nanorippled Graphene

## Komori Group

Electron-phonon coupling plays various roles in solids such as inducing phase transitions and electron energy relaxation. In graphene, it is actually one of the dominant sources of the energy relaxation, and can be locally detected by tunneling spectroscopy with scanning tunneling microscopy as an increase of the tunneling current at the absolute value of the sample-bias voltage corresponding to the phonon energy through an inelastic tunneling (IET) process [1]. We have studied local electron-phonon coupling of a one-dimensionally (1D) nanorippled graphene (3.4 nm period) [2] .

The sample was prepared on a vicinal SiC(0001) substrate by thermal decomposition in an Ar atmosphere. Local atomic and electronic structures of the graphene were characterized using scanning tunneling microscopy/spectroscopy (STM/STS), and the phonon signals were locally detected by IET spectroscopy.

Figure 1 shows STM images of the surface, which consists of terraces and macrofacets of 27° off from the (0001) surface. The macrofacet surface is covered by continuous graphene with 1D periodic undulation. The 1D super periodicity of the graphene is evidenced by satellite band signals in the angle-resolved photoemission spectroscopy (ARPES) images of the graphene Dirac band from the macrofacet shown in Fig. 2(a). ARPES signals from the second-layer graphene were clearly observed using 40.8 eV photons as in Fig. 2 (b). Thus, the interface between surface graphene and the SiC substrate consists of alternate nanoribbons of graphene and the carbon buffer layer.

In the STS measurement, we observed IET signals due to phonons in the vertical direction of the graphene plane. The signal intensity periodically oscillates in the 1D undulation direction of graphene with the same periodicity. This means that the intensity of the inelastic scattering due to the electron-phonon interaction oscillates in the tilting direction of the macrofacet. Since the STM image of the graphene surface looks uniform, we conclude that the IET intensity oscillation is attributed to the subsurface interface layer. The tunneling electrons are easy to move from the surface graphene to the second layer graphene nanoribbon, but not



(a) Terrace & macrofacet

(b) Graphene on terrace

(c) Graphene on macrofacet

macrofacet

65 nm

3.0 nm

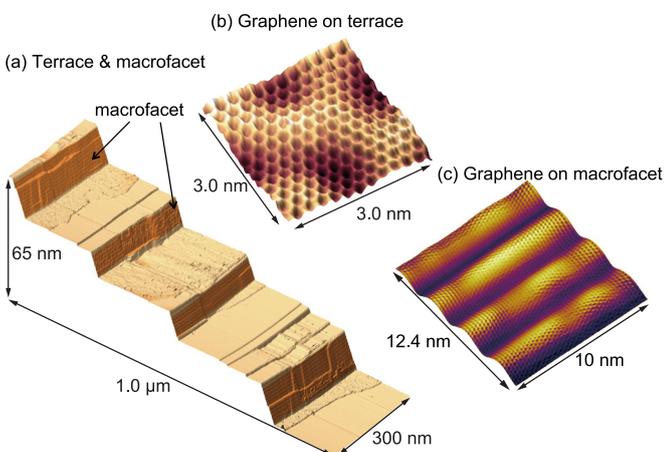3.0 nm

12.4 nm

10 nm

1.0 µm

300 nm

Fig. 1. STM images of graphene grown on a vicinal SiC(0001) substrate. (a) Wide image indicating terrace and macrofacet structure of the substrate. 1D undulation can be seen on the macrofacets (b) Graphene honeycomb lattice on the terrace. (c) 1D periodically-undulated graphene on the macrofacet.
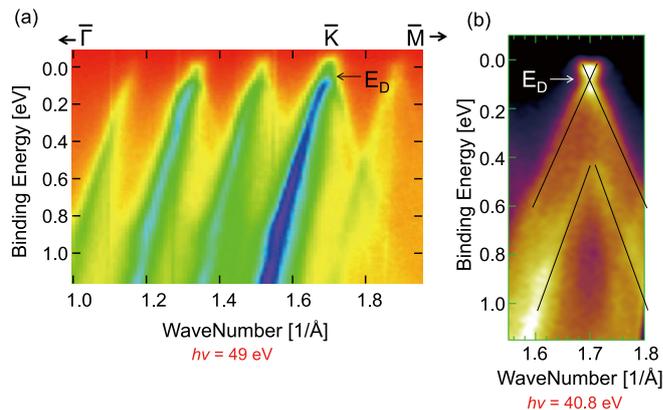


Fig. 2. ARPES spectra using 49 eV (a) and 40.8 eV (b) photons. Four replica bands are seen as well as the true graphene Dirac band in (a). The separation of the bands is consistent with the period of the 1D undulated graphene. Using 40.8 eV photons, the signal from the subsurface graphene nanoribbons was detected in (b).

to in the buffer layer because of the long interlayer distance. Due to this difference, the probability that tunnel electrons interact with the phonon system is larger on the buffer layer.

**References**
[1] C.-H. Kim *et al.,* Nature Phys. **4**, 213 (2008).
[2] K. Ienaga *et al*., Nano. Lett. **17**, 3527 (2017).

**Authors**
K. Ienaga, T. Miyamachi, K. Yaji, K. Fukuma[a], A. Visikovsliy[a], S. Tanaka[a], and F. Komori
[a]Kyushu University

# Orbital Ordering Visualized by Scanning Tunneling Microscopy

## Hasegawa Group

Orbital-related physics attracts growing interest in condensed matter research and there have been reported topics ranging from orbital orders and colossal magnetoresistance to various non-trivial new phenomena, such as superconductivity mediated by orbital fluctuations, orbital Kondo effect, and ordering of multipole moments. However, orbital sensitive probes have so far proved quite limited and there has been no direct access to the real-space form of the orbitals. On the other hand, recent progress of scanning tunneling microscopy (STM) enables the orbital-selective tunneling depending on the tip-sample distance (TSD). Here, we utilize the orbital sensitivity of STM to investigate the surface of the well-known heavy fermion superconductor $CeCoIn_5$ and successfully unveil a surface-assisted cobalt $d$-orbital order with the support of first principles calculations [1]. Our finding suggests that the surface-assisted orbital ordering could be ubiquitous in transition metal oxides, heavy fermion superconductors, and other materials but has been overlooked.

Our target material $CeCoIn_5$ is naturally born at the quantum critical point having the unconventional d-wave superconducting phase below the critical temperature $T_C = 2.3$ K. The compound has a tetragonal structure composed of three different layers, cerium (Ce)-indium (In), In, and cobalt (Co) layers, stacked in the order of CeIn-In-Co-In-CeIn along the c axis as shown in the left panel of Fig. 1. The second highest critical temperature among heavy fermion superconductors and the availability of high-quality single
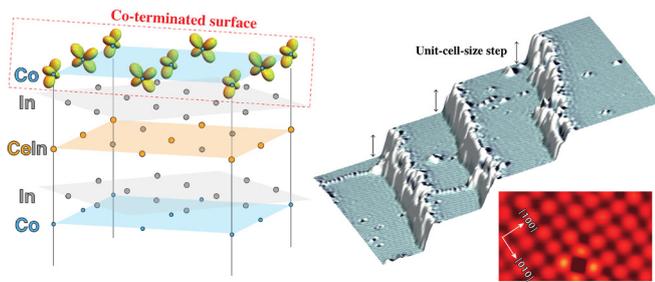
Fig. 1. (left panel) Schematic of the tetragonal crystal structure of $CeCoIn_5$ with $d_{xz}$-$d_{yz}$ orbital order at the topmost cobalt plane. (right-top panel) Overview of a typical cleaved surface in this study. Narrow terraces are separated by a step of the unit cell along c axis. The topographic images are colorized with their derivatives to emphasize the atomically resolved lattice structures. (right-bottom panel) Typical atomically resolved STM image taken on the surface.

crystals make this compound the most investigated heavy fermion superconductor.

We cleaved this compound in ultra-high-vacuum condition and measured with low-temperature STM. The right-top panel of Fig. 1 is a typical overview image of the Co-terminated surface of $CeCoIn_5$. Atomically-flat terraces are separated with steps whose height are the unit-cell size along the c axis. In the normal tunneling conditions; when the tip is far away from the surface, spherical-shaped cobalt atoms are visualized on the square lattice as shown in the right-bottom panel of Fig. 1. This atomic shape is coming from states derived from the Co $4s$ orbital, which has the longer decay into the vacuum than the $3d$ orbitals. By decreasing TSD extremely to be sensitive to $3d$ orbitals, we witness drastic changes of the Co atomic shapes as shown in Fig. 2. The Co atomic shape changes from the spherical shape to the elongated dumbbell by decreasing TSD. The elongated directions are the [100] or the [010] directions, which alternate between the adjacent atomic sites. This observation is well reproduced with first principles calculations (the right side of the right panel) and interpreted as the surface-assisted $d_{xz}$-$d_{yz}$ orbital ordered state.

This surface-assisted orbital order has been overlooked by surface insensitive measurement techniques and even by STM. Since we have experience in STM measurements with very small tip-sample distances [2], which is the first experiment successfully achieving point contact imaging with even smaller tip-sample distances than the present work, we were able to uncover this new phenomenon, achieving the first direct visualization of orbital order in real space. The surface-assisted orbital order is a new concept, but it is not exclusive for heavy fermion compounds. This kind of orbital order should show up in many other compounds containing orbital degrees of freedom in bulk. Therefore, our finding has

major relevance not only in heavy fermion physics but also in the broad range of condensed matter physics and material science. Although we have yet to clarify this, there could very well be links between this orbital order and the bulk properties of the compounds. Applying this technique to the other compounds that have been investigated heavily but still poorly understood, such as $URu_2Si_2$, we might find a new avenue to explore unsolved mysteries.

### References
[1] H. Kim, Y. Yoshida, C-.C. Lee, T.-R. Chang, H.-T. Jeng, H. Lin, Y. Haga, Z. Fisk, and Y. Hasegawa, Science Advances **3**, eaao0362 (2017).
[2] H. Kim and Y. Hasegawa, Phys. Rev. Lett. **114**, 206801 (2015).

### Authors
H. Kim, Y. Yoshida, C.-C. Lee[a], T.-R. Chang[b], H.-T. Jeng[c, d], H. Lin[a], Y. Haga[e], Z. Fisk[e, f], and Y. Hasegawa
[a]National University of Singapore
[b]National Cheng Kung University
[c]National Tsing Hua University
[d]Institute of Physics, Academia Sinica
[e]Japan Atomic Energy Agency
[f]University of California, Irvine

# Hole Trapping in SrTiO₃

## Lippmaa Group

Well-known perovskite titanates such as $SrTiO_3$ and $BaTiO_3$ generally exhibit $n$-type semiconductor behavior due to the prevalence of oxygen vacancies that can form under common synthesis conditions. Each oxygen vacancy donates two electrons and in $SrTiO_3$, for example, a metallic state appears at a relatively low carrier density of about $10^{17}$ cm$^{-3}$. Besides oxygen vacancies, cation vacancies may also form in titanates. In particular, formation of $A$-site cation (Sr, Ba) vacancies is energetically favorable and leads to effective acceptor doping. It is known experimentally that the Fermi level in intrinsic $SrTiO_3$ is close to the conduction band bottom, i.e., the material is effectively an $n$-type wide-gap semiconductor, which means that compensation by acceptor-type cation vacancies is not observed and the cation defect densities must be much lower than $10^{17}$ cm$^{-3}$, which can be ignored in conventional transport analysis.

The situation is very different when optoelectronic applications are considered, where photogenerated carrier mobility, trapping, and lifetime are important parameters. The presence of cation defects needs to be considered because the presence of acceptor states close to the top of the valence band can influence hole trapping and thus the recombination rate of photogenerated non-equilibrium carriers. Unfortunately, typical optical absorption or photo-electron emission spectroscopic techniques cannot detect such low-density vacancy states. We have therefore developed a technique based on measuring the infrared quenching effect on photocurrent, which is illustrated in Fig. 1. Carriers are generated by ultraviolet light across the band gap and the photocurrent is measured as a function of temperature. The magnitude of the photocurrent is determined by the recombination rate of photocarriers, which depends on whether holes are trapped or delocalized. Hole trapping normally occurs at low temperatures in the presence of acceptor defects, reducing the recombination rate and increasing the photocurrent, as can be seen at around 35 K in Figs. 1(a,b). If a crystal is illuminated with ultraviolet and infrared light at the same time, the holes trapped at so-called sensitizing centers can
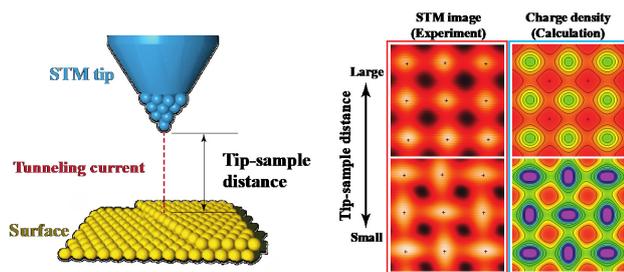


Fig. 2. STM images of Co-terminated surface with large and small tip-sample distances with corresponding calculated density-of-state mappings based on first principles calculations. The experimental observations are well reproduced with the calculations demonstrating the emergence of $d_{xz}$-$d_{yz}$ orbital order on the surface.
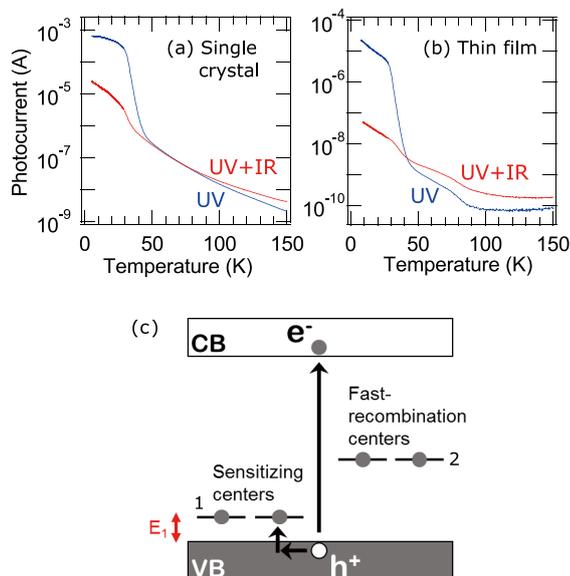
Fig. 1. Photocurrent in SrTiO$_3$ as a function of temperature under ultraviolet (UV) or simultaneous ultraviolet and infrared (UV+IR) excitation for (a) bulk crystal and (b) thin film. Infrared quenching of photocurrent can be seen below 35 K. (c) Energy level diagram illustrating the localization of photogenerated holes. Photocurrent quenching occurs when the trapped holes are released by infrared light illumination.

be detrapped and the photocurrent drops due to the increased recombination rate. The energy level diagram illustrating this mechanism is shown in Fig. 1(c). The delocalization of holes depends on the depth of the acceptor state, $E_1$, and the temperature. For Sr vacancy defects in SrTiO$_3$, thermal detrapping occurs between 30 K and 90 K, depending on how the crystal was grown. The value of $E_1$ can be obtained by fitting the photocurrent temperature dependence close to the infrared quenching transition temperature. For the SrTiO$_3$ samples used in this study, $E_1$ is about 60 meV.

Bulk SrTiO$_3$ crystals are grown by the Verneuil method and always contain Sr vacancies due to the high crystal growth temperature. Thin films are usually grown at much lower temperatures and it is thus not clear if the Sr vacancy density would be similar to bulk crystals or not. As shown in Fig. 1(b), the photocurrent behavior of a thin film grown at 1200°C is indeed similar to the bulk behavior and the infrared quenching effect can be clearly observed. No infrared quenching is observed in films grown at lower temperatures, but the photocurrent is also much lower due to higher density of lattice defects and strong carrier trapping.

The work shows that attempts to improve titanate lattice quality by increasing the crystal growth temperature can be counter-productive in optoelectronic applications due to the spontaneous formation of cation vacancies at higher temperatures. We demonstrate that photocurrent measurement with multiple light sources can be a simple technique for verifying the presence of cation defects that can be difficult or impossible to detect by other spectroscopic techniques [1].

## References
[1] N. Osawa, R. Takahashi, and M. Lippmaa, Appl. Phys. Lett. **110**, 263902 (2017).

## Authors
N. Osawa, R. Takahashi, and M. Lippmaa

# Gas Exposure Effects on Monolayer Pentacene Field-Effect Transistor Studied by Using Non-Invasive Liquid-Metal GaIn Probes

## Yoshinobu Group

The interactions of gaseous molecules with organic field effect transistors (OFETs) play a crucial role in the electronic transport property. Chemical interactions including oxidization are a serious issue for degradation of long-term stability of organic devices. Physical adsorption can also modify electronic states of OFETs. Gaseous molecules may diffuse into OFET film through defect sites such as grain boundaries, resulting in a change in the film structure and/or the formation of a gap state.

Recently, we have developed the non-invasive liquid-metal GaIn four-probe measurement method for the FET properties of organic monolayer and thin films [1, 2]. In this Research Highlight, we report that the electrical transport property of monolayer pentacene is highly sensitive to a small amount of exposure to O$_2$, N$_2$ and Ar gases using independently-driven four GaIn probes [2]. Liquid metal GaIn probes have been used as non-invasive conductivity electrodes for monolayer OFET films in a vacuum chamber (Fig. 1). We carried out the fabrication of monolayer pentacene and the four-probe measurement without exposure to atmospheric air. Four GaIn probes were used *in situ* to measure conductivity in the channel separately from the overall characteristics including contact resistance at the electrode probes [3].

The experimental results show that O$_2$ exposure of 1 L (10$^{-6}$ Torr s) reduces mobility to 8% of the original value in the monolayer film, and the reduction is irreversible at room temperature, i.e., mobility does not recover its original value after the evacuation of gaseous molecules (Fig. 2). Since chemically inert gases of N$_2$ and Ar also reduce the mobility, physisorption of gaseous molecules should be involved in these gas exposure effects. For a 3 ML pentacene film, O$_2$ exposure also reduces its mobility, but the mobility is saturated at 70% of the original value between 10 L to O$_2$
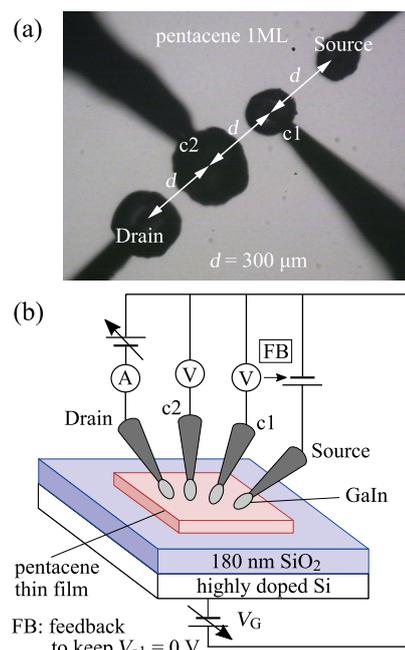


Fig. 1. (a) Optical microscope image of four GaIn probes contacted with 1 ML pentacene. (b) Schematic of the electrical circuits.
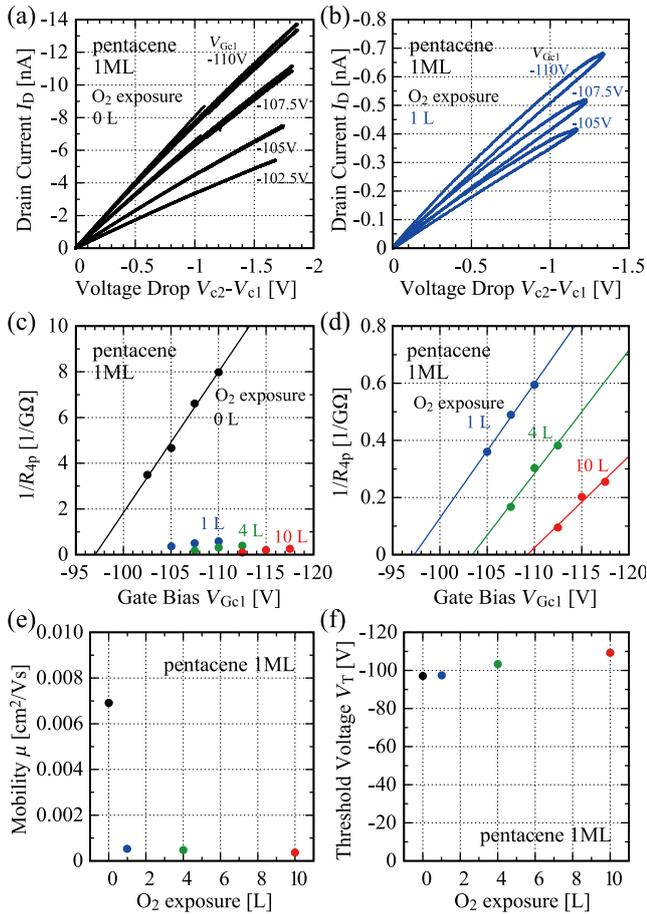
Fig. 2. Four-probe I−V curves (a) before and (b) after $O_2$ exposure measured with the probe alignment shown in Figure 1(a). (c) and (d) Inverse of four-probe resistance $1/R_{4p}$ as a function of gate to channel bias $V_{Gc1}$, respectively. (e) Estimated mobility and (f) threshold voltage.

atmosphere. Thus, we assume that physical adsorption of gaseous molecules is important for the initial gas exposure effects, because chemically inert gases of $N_2$ and Ar also reduced the mobility in monolayer pentacene. Taking these findings together with the results of photoelectron spectroscopy and atomic force microscopy measurements, the reduction in mobility can be attributed to the physisorption of gases at grain boundaries formed by the coalescence of pentacene monolayer islands [2].

**References**
[1] S. Yoshimoto, K. Takahashi, M. Suzuki, H. Yamada, R. Miyahara, K. Mukai, and J. Yoshinobu, Appl. Phys. Lett. **111**, 073301 (2017).
[2] S. Yoshimoto, R. Miyahara, Y. Yoshikura, J. Tang, K. Mukai, and J. Yoshinobu, Organic Electronics **54**, 34 (2018).
[3] S. Yoshimoto, T. Tsutsui, K. Mukai, and J.Yoshinobu, Rev. Sci. Instrum. **82**, 093902 (2011).

**Authors**
S. Yoshimoto, R. Miyahara, Y. Yoshikura, J. Tang, K. Mukai, and J.Yoshinobu

# Large Magneto-Optical Kerr Effect and Imaging of Magnetic Octupole Domains in the Non-Collinear Antiferromagnetic Metal Mn₃Sn

## Nakatsuji Group

When a polarized light beam is incident upon the surface of a magnetic material, the reflected light undergoes a polarization rotation. This magneto-optical Kerr effect (MOKE) has been intensively studied in a variety of ferro- and ferrimagnetic materials because it provides a powerful probe for electronic and magnetic properties as well as for various applications including magneto-optical recording. Recently, there has been a surge of interest in antiferromagnets (AFMs) as prospective spintronic materials for high-density and ultrafast memory devices, owing to their vanishingly small stray field and orders of magnitude faster spin dynamics compared to their ferromagnetic counterparts [1]. In fact, the MOKE has proven useful for the study and application of the antiferromagnetic (AF) state. Although limited to insulators, certain types of AFMs are known to exhibit a large MOKE, as they are weak ferromagnets due to canting of the otherwise collinear spin structure [2]. In the fully compensated collinear AFMs, where the MOKE is usually absent, quadratic magneto-optical effects such as the Voigt effect can be useful to determine the Néel vector [3]. On the other hand, recent theoretical and experimental progress has revealed that systems such as certain spin liquids and non-collinear AFMs can exhibit a large anomalous Hall effect (AHE) in zero applied magnetic field despite a vanishing magnetization [4, 5]. Because the AHE has the same symmetry requirements as the MOKE [6], it is possible that the same class of AFMs may exhibit a Kerr rotation. Thus, the recent experimental discovery of a large AHE in the non-collinear AFM Mn₃Sn [5], which is recently reported to be the first example of a Weyl magnet [7], as well as its
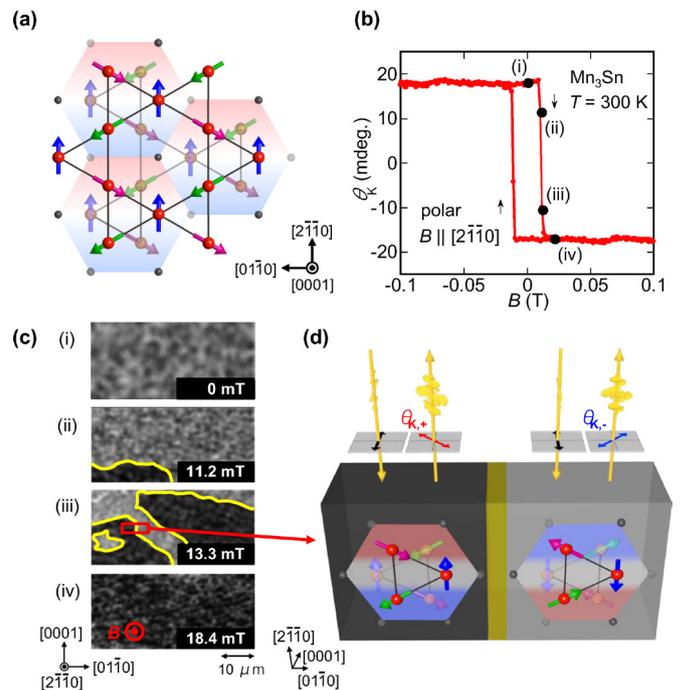


Fig. 1. (a) Cluster magnetic octupole ordering of Mn₃Sn. Large red (small dark grey) and large transparent orange (small transparent grey) spheres represent Mn (Sn) atoms forming kagome planes at $z = 0$ and 1/2, respectively. The Mn magnetic moments (arrows) lie in the (0001) plane and form an inverse triangular spin structure. Different colored arrows represent three sublattices. The spin structure on the kagome bilayers can be considered as ferroic order of cluster magnetic octupoles. (b) Field $B$ dependence of the polar magneto-optical Kerr rotation angle $\theta_K$ for the $(2\bar{1}\bar{1}0)$ plane in $B \parallel [2\bar{1}\bar{1}0]$. (c) Evolution of the antiferromagnetic domains of the $(2\bar{1}\bar{1}0)$ plane as a function of $B \parallel [2\bar{1}\bar{1}0]$ ($-21\,mT \leq B \leq 21\,mT$). The imaging area is $25\,\mu m \times 50\,\mu m$. Grey and black regions correspond to positive and negative values of the MOKE signal. (d) Schematic illustration of two regions with different MOKE image contrasts (grey/black areas) due to opposite signs of the Kerr angles $\theta_{K,-/+}$, corresponding to two types of cluster magnetic octupole domains that have inverse triangular spin structures with opposite spin directions within the (0001) plane. The two regions should be separated by a domain wall (yellow area).

soft response to a magnetic field give promise for a potentially large MOKE character.

$Mn_3Sn$ is a hexagonal antiferromagnet (space group: $P6_3/mmc$), which has the ABAB sequence of the Mn kagome layer along [0001] and exhibits the non-collinear AF spin structure below the Néel temperature of $T_N \sim 430$ K [4]. This three-sublattice AF state on the kagome bilayers can be viewed as "ferroic ordering of cluster magnetic octupoles" (Fig. 1(a)) [8]. In addition to this dominant order parameter, the moments cant slightly in the plane to produce a small net ferromagnetic (FM) moment of $\sim 0.002$ $\mu_B$/Mn within the (0001) plane. Although the subdominant FM order is not responsible for the AHE [4] (and MOKE as we discuss below), it is essential (together with concomitant weak in-plane anisotropy) for magnetic field to control the AF spin structure. This is demonstrated, for example, by the sign reversal of the AHE using a small applied field of $B \sim 15$ mT within the (0001) plane, corresponding to the in-plane rotation of the Mn moments.

We carried out field-swept measurements of the polar MOKE using the $Mn_3Sn$ ($2\bar{1}\bar{1}0$) plane with a $\lambda = 660$ nm linearly polarized laser at 300 K. Significantly, a large zero-field Kerr rotation angle $\theta_K \sim 20$ mdeg and a clear square hysteresis loop are observed in $B \parallel [2\bar{1}\bar{1}0]$ (Fig. 1(b)), which is comparable to the case for ferromagnetic materials. The coercive field $B_C \sim 12$ mT is consistent with the hysteresis curve obtained in $\rho_H(B)$, indicating that the magnetic properties at the surface are nominally identical to those in the bulk [4]. Moreover, our polar MOKE spectroscopy and first-principles calculation for the frequency dependence of the Kerr rotation $\theta_K(\omega)$ have clarified that ferroic ordering of magnetic octupoles in the non-collinear Néel state may cause a large MOKE even in its fully compensated AF state. The large MOKE signal without spin magnetization sharply contrasts with the previously known AF insulator cases where weak ferromagnetism has been believed to be essential for the presence of the MOKE. This large MOKE further allows imaging of the magnetic octupole domains and their reversal induced by $B$. Figure 1(c) presents a series of the polar MOKE images of the $Mn_3Sn$ ($2\bar{1}\bar{1}0$) plane under $B \parallel [2\bar{1}\bar{1}0]$ ($-21$ mT $\leq B \leq 21$ mT) which obtained at the points (i)-(iv) in Fig. 1(b). Here, grey and black colors correspond to positive and negative values of the polar MOKE signal parallel to the $[2\bar{1}\bar{1}0]$ direction originating from the two types of the cluster magnetic octupole domain in Fig. 1(d). This is the first observation of domain reversal in an AF metal and of magnetic octupole domain reversal by MOKE microscopy [7]. The large MOKE observed in an AF metal should open new avenues for the study of domain dynamics as well as spintronics using AFMs.

References
[1] T. Jungwirth *et al.*, Nat. Nanotech. **5**, 231 (2016).
[2] F. J. Kahn *et al.*, Phys. Rev. **186**, 891 (1969).
[3] V. Saidl *et al.*, Nat. Photon. **11**, 91 (2017).
[4] Y. Machida *et al.*, Nature **463**, 210 (2010); H. Chen *et al.*, Phys. Rev. Lett. **112**, 017205 (2014); N. Kiyohara, T. Tomita, and S. Nakatsuji, Phys. Rev. Applied **5**, 064009 (2016).
[5] S. Nakatsuji, N. Kiyohara, and T. Higo, Nature **527**, 212 (2015).
[6] W. Feng *et al.*, Phys. Rev. B **92**, 144426 (2015).
[7] K. Kuroda and T. Tomita *et al.*, Nat.Mater. **16**, 1090 (2017).
[8] T. Higo, H. Man, D. Gopman, L. Wu, T. Koretsune, O. van 't Erve, Y. Kabanov, D. Rees, Y. Li, M.-T. Suzuki, S. Patankar, M. Ikhlas, C. L. Chien, R. Arita, R. Shull, J. Orenstein, and S. Nakatsuji, Nat. Photon. **12**, 73 (2018).

Authors
T. Higo, H. Man, D. Gopman[a], L. Wu[b], T. Koretsune[c,d], O. van 't Erve[e], Y. Kabanov[a], D. Rees[b], Y. Li[f], M.-T. Suzuki[c,d], S. Patankar[b], M. Ikhlas, C. L. Chien[f], R. Arita[c,g], R. Shull[a], J. Orenstein[b], and S. Nakatsuji

[a]National Institute of Standards and Technology
[b]University of California, Berkeley
[c]RIKEN-CEMS
[d]Tohoku University
[e]U.S. Naval Research Laboratory
[f]Johns Hopkins University
[g]The University of Tokyo

# Strongly Correlated Zero-Gap Semiconductor $Pr_2Ir_2O_7$

## Nakatsuji Group

In the field of the solid state physics, materials exhibiting novel physical properties are vigorously explored. Zero-gap semiconductors are one fascinating group of materials where topological functionalities lead to high carrier mobility and the quantum Hall effect. It is known that electrons behave as if they are massless in materials such as graphene because of the linear band dispersion near the point where the valence and the conduction bands come in contact with each other. For graphene, new phenomena were discovered one after another and it became the subject of the Nobel Prize in Physics in 2010. So far, the physics of zero-gap semiconductors have only been studied in materials where the interaction between electrons is weak.

An example of a zero-gap structure is a Luttinger semimetal with quadratic band touching whose band dispersion is parabolic near the band touching point as illustrated in Fig. 1. It was predicted more than 40 years ago that materials in a Luttinger semimetal state would show novel electronic states because of the strong electronic correlations that are unobtainable in conventional metals. However, in materials known so far, such as $\alpha$–Sn and HgTe, it has been difficult to identify experimentally the effects of electronic correlations because the effective mass of electrons is small and hence the electronic correlations are weak.

To clarify the effect of the strong electronic correlations, we focused on $Pr_2Ir_2O_7$ [1]. It is already known that $Pr_2Ir_2O_7$ is a Luttinger semimetal with quadratic band touching and that the effective mass of electrons is about 6 times larger than the mass of the free electron in vacuum [2]. We therefore carried out a terahertz spectroscopy study on the $Pr_2Ir_2O_7$ thin films and observed a very large dielectric constant of about 180 at a temperature of 5 K as shown in Fig. 2 [3]. This value is several tens of times larger than
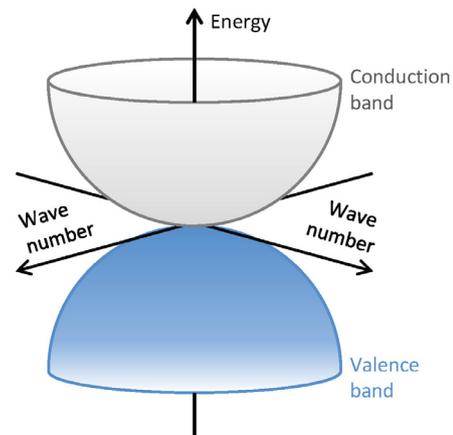


Fig. 1. Band structure of a Luttinger semimetal, which is a zero-gap semiconductor. The valence band, which is filled with electrons (blue spheres) and the empty conduction band both have a three-dimensional parabolic shape, and are in contact with each other at a single point close to the Fermi level.
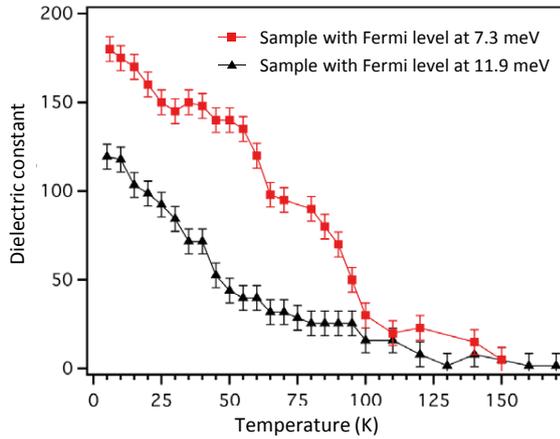
Fig. 2. Temperature dependence of the dielectric constant. The low-temperature value is several tens of times larger than that of known zero-gap semiconductors (e.g. α–Sn and HgTe). The dielectric constant becomes larger when the Fermi level approaches the band touching point.

that of zero-gap semiconductors (e.g. α–Sn and HgTe) known so far. Additionally, in a Luttinger semimetal state, the dielectric constant is a measure of the scale of electronic correlations. By using this fact, when the magnitude of the electronic correlations is estimated from the dielectric constant, the scale of electronic correlations is about 2 orders of magnitude larger than the kinetic energy.

We have thus demonstrated that electronic correlations are indeed very strong in a Luttinger semimetal with quadratic band touching. In the future, it is expected that further understanding of the role of electronic correlations in determining the physical properties of zero-gap semiconductors will lead to the creation of novel metallic states and new functional materials.

**References**
[1] T. Ohtsuki, Z. Tian, A. Endo, M. Halim, S. Katsumoto, Y. Kohama, K. Kindo, S. Nakatsuji, and M. Lippmaa, arXiv:1711.07813 (2017).
[2] T. Kondo, M. Nakayama, R. Chen, J. J. Ishikawa, E.-G. Moon, T. Yamamoto, Y. Ota, W. Malaeb, H. Kanai, Y. Nakashima, Y. Ishida, R. Yoshida, H. Yamamoto, M. Matsunami, S. Kimura, N. Inami, K. Ono, H. Kumigashira, S. Nakatsuji, L. Balents, and S. Shin, Nat. Commun. **6**, 10042 (2015).
[3] B. Cheng, T. Ohtsuki, D. Chaudhuri, S. Nakatsuji, M. Lippmaa, and N. P. Armitage, Nat. Commun. **8**, 2097 (2017).

**Authors**
T. Ohtsuki, B. Cheng[a], D. Chaudhuri[a], S. Nakatsuji, M. Lippmaa, and N. P. Armitage[a]
[a]Johns Hopkins University

# Large Anomalous Nernst Effect at Room Temperature in a Chiral Antiferromagnet

## Nakatsuji Group

The anomalous Nernst effect (ANE) is the thermoelectric counterpart to the anomalous Hall effect (AHE), that is, when one applies thermal gradient to a ferromagnetic conductor, spontaneous voltage drop will appear perpendicular to both the applied heat current and the direction of the magnetization. In earlier studies, these two phenomena have been considered to be proportional to the magnetization. However, modern theory of transport properties based on Berry phase has opened up the possibilities of observing anomalous transport effects in materials with zero net magnetization, such as in antiferromagnets (AFM) [1].
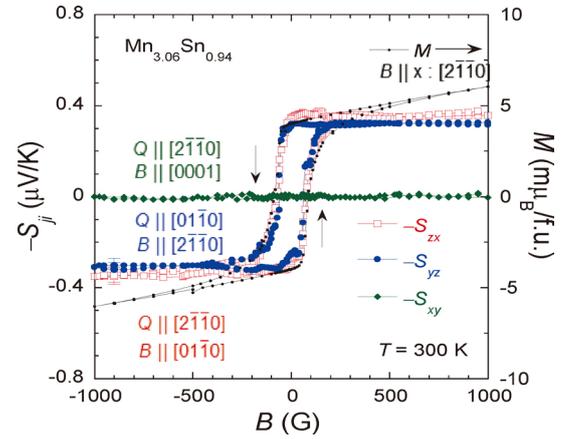


Fig. 1. Anisotropic magnetic field dependence of the Nernst signal $S_{ji}$ ($i, j = x$: [$2\bar{1}\bar{1}0$], $y$: [$01\bar{1}0$], $z$: [0001]) in $Mn_3Sn$.

$Mn_3Sn$ is a metallic AFM crystallizing in the hexagonal structure, with Mn atoms forming a kagome lattice in the $ab$ plane that is stacked along the $c$-axis. Below the Neel temperature of 430 K, Mn spins undergo a transition from a paramagnetic state to a non-collinear, inverse triangular spin structure [2]. The orthorhombic symmetry of this magnetic orders permits an exceedingly tiny in-plane spontaneous magnetization ~ 2$m\mu_B$/Mn to appear, the direction of which can be controlled by a small magnetic field of ~ 200 Oe. Experimentally, $Mn_3Sn$ exhibits large anomalous Hall conductivity in this non-collinear phase, the first case for AFM [3]. In this study, we measured magneto-thermoelectric transport of two off-stoichiometric $Mn_3Sn$ single crystals with slightly different compositions, $Mn_{3+x}Sn_{1-x}$ ($x = 0.06$ and $x = 0.09$). We found that for $Mn_{3.06}Sn_{0.94}$, the anomalous Nernst coefficient $S_{zx}$ is 0.35 μV/K at room temperature (Fig. 1) and reaches 0.6 μV/K at 200 K [4], comparable to the maximum value measured for ferromagnetic metal [5]. This Nernst coefficient is around 100 times larger than what we would naively expect based on the size of its magnetization (Fig. 2).

The anomalous Nernst coefficient $S_{zx}$ is governed by the transverse thermoelectric conductivity $\alpha_{zx}$, which is related to the Hall conductivity $\sigma_{zx}$ through the Mott relation. From this relation, we can infer that ANE can be enhanced when the Berry curvature takes a large value in the vicinity of $E_F$. First-principles calculations suggest the existence of Weyl nodes around $E \approx E_F + 60$ meV at which the Hall conductivity peaks. Moreover, the Mn off-stoichiometry is predicted to provide electron carriers that shift $E_F$ towards the location of the Weyl nodes, which may account for the difference in the magnitude and temperature dependence of the $\sigma_{zx}$ and $\alpha_{zx}$
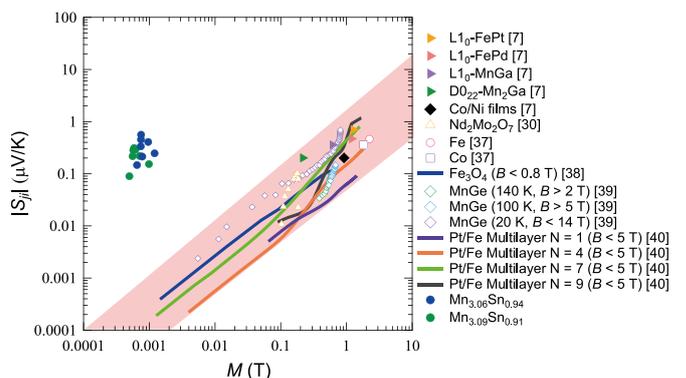


Fig. 2. Magnetization dependence of the spontaneous Nernst signal $|S_{ji}|$ for various ferromagnets and $Mn_3Sn$. References for each listed materials can be found in [4].

between the two measured single crystals.

From a practical standpoint, the anomalous Nernst effect may become useful as the orthogonal orientation between the voltage output and the input heat current allows the construction of thermoelectric module much simpler than the usual pillar-like design utilizing the Seebeck effect. In spite of the small magnitude of the ANE observed in this material, our study may provide a guide for the search of materials more suitable for future thermoelectric power generation.

**References**
[1] M.-T. Suzuki, T. Koretsune, M. Ochi, and R. Arita, Phys. Rev. B. **95** (2017).
[2] T. Nagamiya, and Y. Yamaguchi, Solid State Commu. **42** (1982).
[3] S. Nakatsuji, N. Kiyohara, and T. Higo, Nature **527** (2015).
[4] M. Ikhlas, T. Tomita, T. Koretsune, M.-T. Suzuki, D. Nishio-Hamane, R. Arita, Y. Otani, and S. Nakatsuji, Nat. Phys. **13** (2017).
[5] K. Hasegawa, M. Mizuguchi, Y. Sakuraba, T. Kamada, T. Kojima, T. Kubota, S. Mizukami, T. Miyazaki, and K. Takanashi, Appl. Phys. Lett. **106** (2015).

**Authors**
M. Ikhlas, T. Tomita, T. Koretsune[a], M.-T. Suzuki[a], D. Nishio-Hamane, R. Arita[a], Y. Otani, S. Nakatsuji
[a]RIKEN-CEMS

# Effects of Pressure and Magnetic Field on Superconductivity in ZrTe₃: Local Pair-Induced Superconductivity

## Uwatoko Group

Up to now, the coexistence and competition between charge density waves (CDWs) and superconductivity (SC) have attracted much attention in transition-metal di- and trichalcogenides. Among these compounds, $ZrTe_3$ shows the highly anisotropic SC transition, where the resistance along the $a$ axis, $R_a$, is reduced at 4 K but those along the $b$ axis, $R_b$, and c' axis, $R_{c'}$ are reduced at 2 K. This unusual behavior can be explained by two scenarios, conventional superconducting fluctuation and SC induced by locally bound electron pairs (local pairs). In the former, the reduction in $R_a$ is attributed to a fluctuation in the bulk SC enhanced by the low dimensionality. In the latter, the transitions of $R_a$ and $R_{b,c'}$ correspond to filamentary (highly one dimensional: 1D) and bulk (3D) SC, which originate from the formation of local pairs, namely bi-polarons, and Cooper pairs induced by the transfer of the local pairs, respectively. However, at this moment, it remains unclear which interpretation is acceptable.

In this work [1], to understand SC in more detail, we discuss the influence of pressure and the magnetic field on the SC, as determined via $R_a$ and $R_b$ measurements. In the measurements, the samples with different current configurations were mounted on the same sample holder and piston-cylinder-type cell, and the data were simultaneously taken.

Figures 1 (a) and (b) show the $R_a$ and $R_b$ at various pressures in the low temperature region, respectively. For $P = 0$ GPa, the $R_a$ drops to zero at 2.2 K, while the $R_b$ decreases to zero at 1.4 K. The highly anisotropic SC transitions are reflected by 1D and bulk nature of the SC. A $P$-$T$ phase diagram can be constructed from the data, as shown in Fig. 1(c). Strikingly, the Tc of the bulk SC also decreases in the same manner as that of the 1D SC. This means that the origin of the bulk SC can be related to that of the 1D SC.

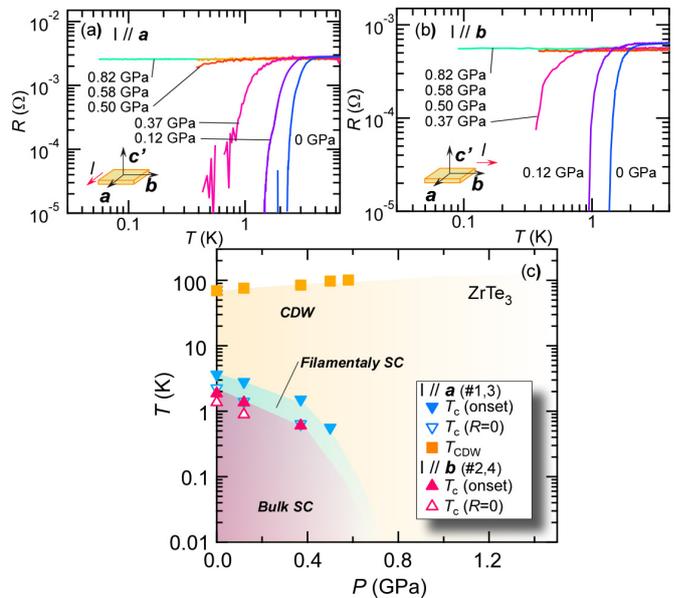To investigate the connection between 1D and bulk SC



Fig. 1. (a),(b): Temperature dependence of the $R_a$ and $R_b$ at various pressures. (c): $P$-$T$ phase diagram of $ZrTe_3$. The blue and red triangles are $T_c$ obtained from the $R_a$ and $R_b$ measurements, respectively.

further, we show that the pressure dependence of $H_{c2}$ of the 1D SC is similar to that of the bulk SC. These similarities indicate that the origin of the bulk SC can be related to that of the 1D SC. Moreover, in analysis of the excess conductivity, our results are in good agreement with the 1D Aslamazov-Larkin model rather than the 3D model, for both the $I$ configurations, suggesting that the conventional fluctuation theory is not appropriate for our data. These findings favor the local-pair-induced SC scenario rather than conventional SC. According to the local-pair induction scenario, 1D SC is attributed to the formation of local pairs owing to a peculiar electronic structure after the CDW transition. The formation of the ordinary Cooper pairs in the bulk SC is induced by the transfer of the local pairs in addition to the 1D SC. This mixing of two kinds of SC, that is, the unconventional mechanism of the bulk SC increases the complexity of the fluctuation phenomena, which may explain the unusual excess conductivity. Moreover, this picture is consistent with the previous studies, such as anomalous behavior of the specific heat [2].

**References**
[1] S. Tsuchiya, K. Matsubayashi, K. Yamaya, S. Takayanagi, S. Tanda, and Y Uwatoko, New J. Phys. **19**, 063004 (2017).
[2] K. Yamaya, S. Takayanagi, and S. Tanda, Phys. Rev. B **85**, 184513 (2012).

**Authors**
S. Tsuchiya[a], K. Matsubayashi[b], K. Yamaya[a], S. Takayanagi[a], S. Tanda[a,c] and Y. Uwatoko
[a]Hokkaido University
[b]The University of Electro-Communications
[c]Center of Education and Research for Topological Science and Technology, Hokkaido University

# High-Tc Superconductivity in FeSe at High Pressure: Dominant Hole Carriers and Enhanced Spin Fluctuations

## Uwatoko Group

The Fermi surface (FS) topology and its interplay with magnetism have been considered key ingredients in under-

standing the mechanism of the iron-based high-$T_c$ superconductors. For the FeAs-based superconductors, the FS typically consists of hole and electron pockets near the Brillouin zone center and corners, respectively. As such, an interband scattering between the hole and electron pockets has been proposed as an important mechanism for electron pairing in the iron-based superconductors, leading to an $s_{\pm}$ pairing state favored by the antiferromagnetic fluctuations. This picture, however, is challenged by the observed distinct FS topology in the FeSe-derived high-$T_c$ (> 30 K) superconductors, including $A_x Fe_{2-y} Se_2$ ($A$ = K, Cs, Rb, Tl), (Li,Fe)OHFeSe, and monolayer FeSe film, in which only the electron pockets are observed near the Fermi level. Therefore, the distinct FS topology between FeAs- and FeSe-based materials has challenged current theories on a unified understanding of the mechanism of iron-based superconductors.

In contrast to electron-doping approaches, the application of high pressure does not introduce extra electron carriers, yet can still enhance $T_c$ of bulk FeSe from 8 K to 38 K near 6 GPa. Our recent high-pressure study on FeSe has shown explicitly that the optimal $T_c$ is achieved when the long-range antiferromagnetic order just vanishes, reminiscent of the situations seen frequently in the FeAs-based superconductors [1]. To make this connection, it is important to have information about the evolution of the FS under high pressure— a regime in which ARPES experiments are impractical, and where quantum oscillation measurements are challenging. Alternatively, we measured the Hall effect under hydrostatic pressures up to 8.8 GPa with the cubic anvil cell technique to gain further insights into the electronic structure evolution of FeSe at high pressure.

The main results are summarized in the phase diagram of Fig. 1. Our results demonstrate that the electrical transport properties of FeSe at high pressures with $T_c^{max}$ = 38.3 K are dominated by the hole carriers, which is in contrast with the known FeSe-derived high-$T_c$ superconductors that are usually heavily electron doped. In addition, we observed an enhancement of Hall coefficient $R_H$ near the critical pressure where the optimal $T_c$ is realized with a simultaneous suppression of the long-range magnetic order. This implies a strong reconstruction of the Fermi surface due to antiferromagnetic order, consistent with the ordering pattern driven by inter-
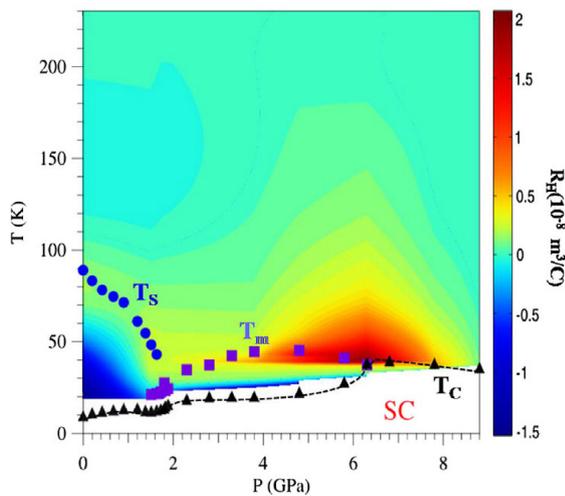
band scattering. Importantly, their results show a continuous path to high-$T_c$ superconductivity in chalcogenides without electron doping.

Thus, our present work can be considered as a significant step forward in making a unified picture on the current understanding of iron-based high-$T_c$ superconductors, specifically by demonstrating that high $T_c$ in FeSe can be achieved with an electronic structure and other characteristics similar to the FeAs-based high-$T_c$ superconductors.

**References**
[1] J. P. Sun, K. Matsuura, G. Z. Ye, Y. Mizukami, M. Shimozawa, K. Matsubayashi, M. Yamashita, T. Watashige, S. Kasahara, Y. Matsuda, J.-Q. Yan, B.C. Sales, Y. Uwatoko, J.-G. Cheng, and T. Shibauchi, Nature Commun. **7**, 12146 (2016).
[2] J. P. Sun, G. Z. Ye, P. Shahi, J.-Q. Yan, K. Matsuura, H. Kontani, G. M. Zhang, Q. Zhou, B. C. Sales, T. Shibauchi, Y. Uwatoko, D. J. Singh, and J.-G. Cheng, Phys. Rev. Lett. **118**, 147004 (2017).

**Authors**
J. P. Sun[a], G. Z. Ye[a,b], P. Shahi[a], J.-Q. Yan[c], K. Matsuura[d], H. Kontani[e], G. M. Zhang[f], Q. Zhou[b], B. C. Sales[c], T. Shibauchi[d], Y. Uwatoko, D. J. Singh[g], and J.-G. Cheng[a]
[a]Institute of Physics, Chinese Academy of Sciences
[b]Yunnan University,
[c]Oak Ridge National Laboratory
[d]The University of Tokyo
[e]Nagoya University
[f]Tsinghua University
[g]University of Missouri

# Pressure induced Bulk Superconductivity in a Layered Transition-Metal Dichalcogenide 1$T$-Tantalum Selenium

## Uwatoko Group

Charge density wave (CDW) and superconductivity (SC) are two low-energy collective excitations in condensed matter physics. The periodic electron density modulations of CDWs and the anisotropic energy gaps at Fermi surface generates multiple commensal electronic orders, either compete or cooperate. The resultant electronic phase
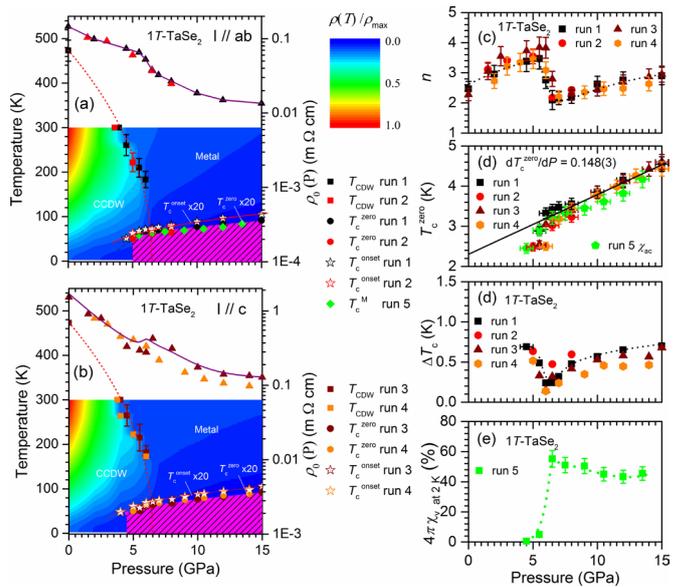


Fig. 1. Phase diagram and Hall coefficient of FeSe. Temperature-pressure phase diagram of FeSe is superimposed by a contour plot of Hall coefficient $R_H$, which is defined as the field derivative of $\rho_{xy}$, $R_H \equiv d\rho_{xy}/dH$, at the zero-field limit at each temperature and pressure. The structural (nematic) transition ($T_s$), pressure-induced magnetic transition ($T_m$), and superconducting (SC) transition ($T_c$) have been determined by the resistivity measurements under pressure [1]. The dashed curve is a guide for the eyes.



Fig. 1. $T$-$P$ diagram and the colors describe the evolution of resistivity; the residual resistivity $\rho_0$ is estimated by fitting $\rho = \rho_0 + AT^n$ up to 20 K. The dashed red line, the red line, the triangle points represent the trend of $T_{CDW}$, $T_c^{onset}$, and $\rho_0$; the parameters versus pressure: (c) the exponent $n$, (d) $T_c^{zero}$ and $T_c^M$, (e) $\Delta T_c$, (f) $4\pi\chi_v$ (2K).
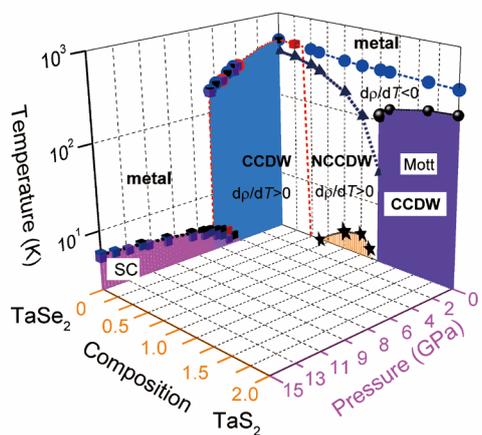
Fig. 2. Phase diagram of 1$T$-TaSe$_2$ in temperature, pressure, and composition. Here, the $d\rho/dT$ is the differential coefficient of resistivity. The red dished line separates the CCDW and NCCDW and the triangle symbols divide the negative and positive $d\rho/dT$.

diagrams have been devoted extensive efforts by controlling external stimulations to reveal the intrinsic physics.

Layered transition-metal dichalcogenides (TMDs) have been studied for nearly 50 years, but the key factors on the interplay of CDW and SC are far from clear. In one case, the superconducting transition temperature assumes a dome-like shape close to the collapsed CDWs; while in other cases, $T_c$ changes insensitively and/or increases monotonously without domes. In former, the superconducting dome resembles that of unconventional SC neighboring quantum critical point. One scenario is proposed that CDW fluctuation glues superconducting pairs since CDW and SC originate from Fermi surface instabilities and electron-phonon coupling. Howbeit, an opposite scenario is argued that CDW is weakly connected to SC (e.g., 1$T$-TaS$_2$) in 1$T$-TMDs, and the dome-shaped superconducting diagram is far from CDW, which tally with the evidences of conventional single-gapped $s$-wave SC. Additionally, superconducting diagram and the coexisting model of CDW and SC depends on tuning routes even from the same starting point. Some argue that CDW and SC coexist on a macroscopic scale in real space, while others support that the insulating CDW domain walls coexist with superconducting interdomains. It implies that the SCs are distinct in superconducting diagrams generated by different parameters, and the coexisting model of CDW and SC is essential to understand the superconducting mechanism.

1$T$-TaSe$_2$, with a higher commensurate CDWs transition temperature ~ 473 K and a larger unit-cell volume compared to isostructural compounds, has attracted our attention as a starting point to explore SC and reveal the interplay of CDW instability and SC by pressure. In this work, we report a pressure-driven SC in the vicinity of CCDW in TMDs 1$T$-TaSe$_2$ by resistivity and ac susceptibility. The superconducting phase enters at 4.5 GPa and bulk SC emerges along with the collapse of CCDW at a critical pressure $P_c$ ~ 6.5 GPa. Higher than $P_c$, $T_c$ keeps increasing linearly, without a dome-shaped superconducting diagram in our pressure range. $T_c$ reaches ~ 5.3 K at 15 GPa. The comprehensive analysis shows that electronic correlations of CCDW phase open energy gaps, which prohibits coopers pairing; while the superconducting channels and CCDW domain wall coexist in three-dimensions above $P_c$. The evolutions of Fermi surface and the softening of phonon models under pressure are proposed to explain the monotone increase of $T_c$. The findings reveal the interplay of CCDW and SC in 1$T$-TaSe$_2$ by a clean method viz. high-pressure,

and shed light on the underlying superconducting mechanism in the relevant systems.

**Reference**
[1] B. S. Wang, Y. Liu, K. Ishigaki, K. Matsubayashi, J. -G. Cheng, W. J. Lu, Y. P. Sun, and Y. Uwatoko, Phys. Rev. B. (rapid) **95**, 220501(R) (2017)

**Authors**
B. S. Wang[a], K. Ishigaki, K. Matsubayashi, Y. Liu[a], W. J. Lu[a], Y. P. Sun[a,b], J.-G. Cheng[c], and Y. Uwatoko
[a]Institute of Solid State Physics, CAS
[b]High Magnetic Field Laboratory, CAS
[c]Institute of Physics, CAS

# Bilayer Sheet Protrusions and Vesicle Budding Induced by Chemical Reactions

## Noguchi Group

In living cells, membrane composition continually changes by lipid metabolism. However, the effects of non-constant membrane composition on shape transformations of cells are not understood so well. We have studied membrane shape transformations under hydrolysis and condensation reactions using dissipative particle dynamics simulation [1]. The hydrolysis and condensation reactions result in the formation and dissociation of amphiphilic molecules, respectively as shown in Fig. 1. Because the dissociated hydrophilic and hydrophobic molecules are typically dissolved in surrounding fluids and embedded in the bilayer, we refer to them as the hydrophilic solute (HS) and embedded oil (EO), respectively.

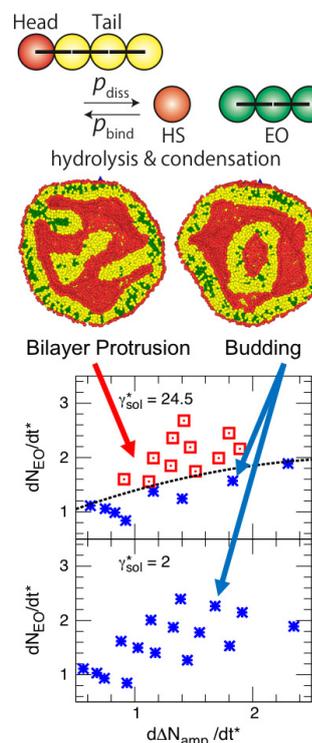Asymmetric reactions between the inner and outer leaflets of a vesicle can transport amphiphilic molecules



Fig. 1. Top: Schematic picture of hydrolysis and condensation reactions. Middle: Snapshots of bilayer sheet protrusions (BP) and budding of vesicles. Bottom: Dynamic phase diagram of shape transformations for the increase rate of the amphiphilic molecular number difference, $\Delta N_{amp} = N_{amp, out} - N_{amp, in}$ between the inner and outer leaflets and the EO synthesis rate $dN_{EO}/dt$ at high viscosity ($\gamma^*_{sol} = 24.5$) and low viscosity ($\gamma^*_{sol} = 2$) of the surrounding fluid at a low reduced volume.

between the leaflets via EO diffusion. We consider high HS density in the inner fluid of the vesicle and investigate how the transport into the inner leaflet changes the membrane shapes. We found that the resulting area difference between the two leaflets induces bilayer sheet protrusion (BP) and budding at low reduced volumes of the vesicles (see the snapshots in Fig. 1), whereas BP only occurs at high reduced volumes. The probabilities of these two types of transformations depend on the shear viscosity of the surrounding fluids compared to the membrane as well as the reaction rates. For high surrounding fluid viscosity, BP formation occurs at high reaction rates, but for low viscosity, budding always occurs before BP formation (see the bottom graphs in Fig. 1). In the budding, the membrane mainly moves normal to the membrane surface, but sliding between two leaflets occurs in BP formation. Thus, the viscosity of the surrounding fluids affects budding more than it does BP formation, while the viscosity in the membrane affects BP formation more. The inhomogeneous spatial distribution of the hydrophobic reaction products forms the nuclei of BP formation, and faster diffusion of the products enhances BP formation. Our results revealed that adjustment of the viscosity is important to control membrane shape transformations.

**Reference**
[1] K. M. Nakagawa and H. Noguchi, Soft Matter **14**, 1397 (2018).

**Authors**
K. M. Nakagawa and H. Noguchi

# Structure of Critical Gel Clusters Formed by Tetra-Functional Polymers

## Shibayama Group

Critical gel clusters are polymer clusters about to become a gel. With a bit more reaction, the critical clusters percolate the system and system changes from fluid "sol" to solid "gel". Polymer gels can be synthesized by various chemical methods: radical polymerization of monomers and crosslinkers, crosslinking the side groups of linear polymer chains by cross-linkers or by irradiation of $\gamma$-rays, coupling end-groups of star polymers, etc. Although there are many different reaction schemes to synthesize gels and different network structure are formed depending on the synthesis
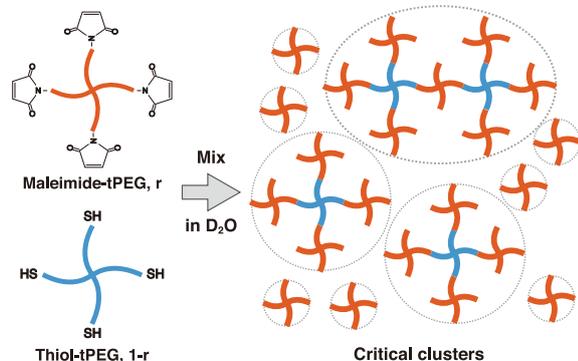


Fig. 1. Schematic for preparation of critical clusters from two different tetra-PEG units carrying mutual reactive end-groups. The excess red polymers cover the surface of the clusters and the reaction automatically stops. With one addition blue units, the clusters will percolate the system. Reprinted with permission from SANS Study on Critical Polymer Clusters of Tetra-Functional Polymers, Xiang Li, Kazu Hirosawa, Takamasa Sakai, Elliot P. Gilbert, and Mitsuhiro Shibayama, Macromolecules 2017 50 (9), 3655-3661. Copyright 2018 American Chemical Society.
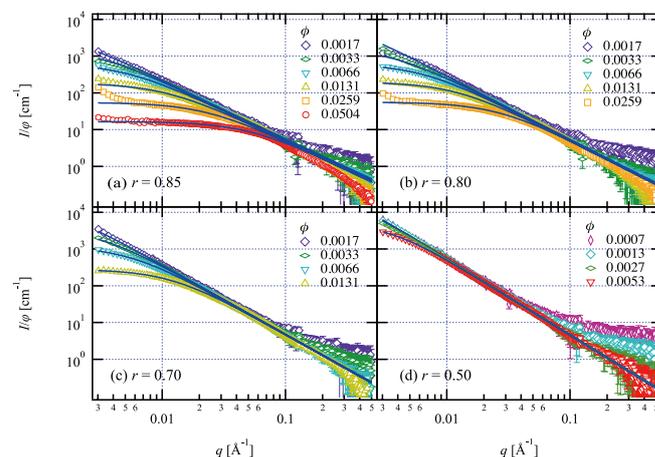


Fig. 2. Scattering profiles of various critical clusters based on the 2D sol-gel phase diagram (a, r=0.85; b, r=0.80; c, r=0.70; d, r=0.5). The profiles of the dilution of each clusters-solution are also shown. The blue curves show the fitting curves of the Bastide-Candau model for scattering profiles of critical clusters solution with finite polymer concentration. Reprinted with permission from SANS Study on Critical Polymer Clusters of Tetra-Functional Polymers, Xiang Li, Kazu Hirosawa, Takamasa Sakai, Elliot P. Gilbert, and Mitsuhiro Shibayama, Macromolecules 2017 50 (9), 3655-3661. Copyright 2018 American Chemical Society.

schemes, a set of universal scaling laws are commonly observed near the gel point, including size-distribution, weight-averaged molecular weight, correlation length.

Although those scaling laws of critical clusters have already been well studied, most of the studies only focused on reaction-conversion-limited clusters (1D phase diagram). The sol-gel phase diagram indeed has three variables: the polymer (or monomer) concentration ($\varphi$), the crosslinker density and the reaction conversion. The lack of studies based on the multi-dimension phase diagram is due to poor reproducibility in forming critical clusters, and difficulty in controlling the polymer concentration and crosslinker density.

Recently, we have successfully synthesized a new type of critical clusters by mixing two different types of tetra-armed poly(ethylene glycol) polymers (tetra-PEGs) with mutual reactive end-groups by offstoichiometric molar ratios (r, r = 0.5 denotes equal stoichiometric ratio) (Fig. 1). By changing the polymer concentration and the molar ratio of two tetra-PEGs (= crosslinker density), we can easily draw a 2D-phase diagram of the critical clusters. Here, we report the structure of these critical clusters studied by means of small angle neutron scattering (SANS) [1-2].

Figure 2 shows the normalized scattering intensity ($I/\varphi$) for different critical clusters formed based on the 2D-phase diagram. The normalized scattering intensity ($I/\varphi$) converged at the $q$-range of the size of prepolymers ($q > 0.1\text{Å}^{-1}$) because all the polymer clusters are formed with the same prepolymers. The slight upper deviation of low concentration sample are due to the low counting statistics of scattered neutrons. In the $q$-range of the size larger than a prepolymer ($q < 0.1\text{Å}^{-1}$), the SANS profiles are well reproduced by the Bastide-Candau model, which is designed for the scattering of critical gel clusters at finite concentration regime. The fractal dimension ($D_s$) of swollen critical clusters and the size-distribution exponent (Fisher exponent, $\tau$) were estimated from the fitting parameters. $D_s$ was a unique value (= 2.0 ± 0.1) irrespective of preparation condition while the values of $\tau$ increased from 1.90 to 2.25 with deviating $r$ from the stoichiometric ratio ($r = 0.5$), suggesting that smaller polymer clusters tend to be formed

in off-stoichiometric ratio. This study clearly shows that the fractal structure of the critical clusters is universal irrespective of the synthesized condition, while the size-distribution of critical clusters is a tunable parameter, which was unexpected by the classical percolation theory.

### References
[1] X. Li, K. Hirosawa, T. Sakai, E. P. Gilbert, and M. Shibayama, Macromolecules **50**, 3655 (2017).
[2] K. Hayashi, F. Okamoto, S. Hoshi, T. Katashima, D. C. Zujur, X. Li, M. Shibayama, E. P. Gilbert, U.-I. Chung, S. Ohba *et al.*, Nat. Biomed. Eng. **1**, 0044 (2017).

### Authors
X. Li and M. Shibayama

# Dynamics of Alkylammonium-Based Ionic Liquids with Plastic-crystalline Phases

## Yamamuro Group

One of the characteristic and interesting features of ionic liquids (ILs) is nanometer-sized structure (nanostructure). For example, imidazolium-based ILs (ImILs) have nanostructures consisting of the polar-domains with imidazolium rings and anions and the non-polar domains with alkyl-chains of the cations. We have revealed that the nanostructure is essentially the same as that of a liquid-crystalline (LC) phase [1-3, 5] and investigated the dynamics of ImILs by means of quasielastic neutron scattering (QENS) [1, 2, 4, 5]. Recently, Yamada et al. found that some of alkylammonium-based salts, which are another popular ILs, have plastic-crystalline (PC) phases that are the counterparts to the LC phase; i.e., the LC phase has an orientationally-ordered positionally-disordered structure, while the PC phase has an orientationally-disordered positionally-ordered one.

We have measured the DSC, neutron diffraction (ND) and QENS data of methyldiethylisopropyl-ammonium bis(trifluoromethylsulfonyl)imide (abbreviated as $N_{1223}$'$Tf_2N$) and the methyl-ethylpropylisopropylammonium salt ($N_{1233}$'$Tf_2N$) in a temperature range between 4 and 400 K. The former cation is more spherical and non-chiral while the latter more ellipsoidal and chiral. The DSC and ND works revealed that both of two samples have, in the order of deceasing temperature, liquid (L), PC1, PC2 and crystalline (C) phases; PC1 may be a normal isotropic PC phase and PC2 an anisotropic PC phase where the cations undergo more restricted rotations. The QENS data were collected in a
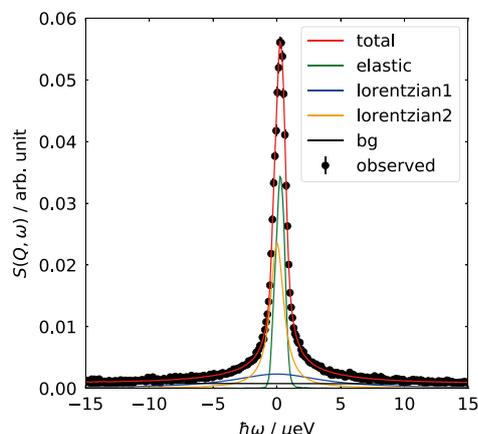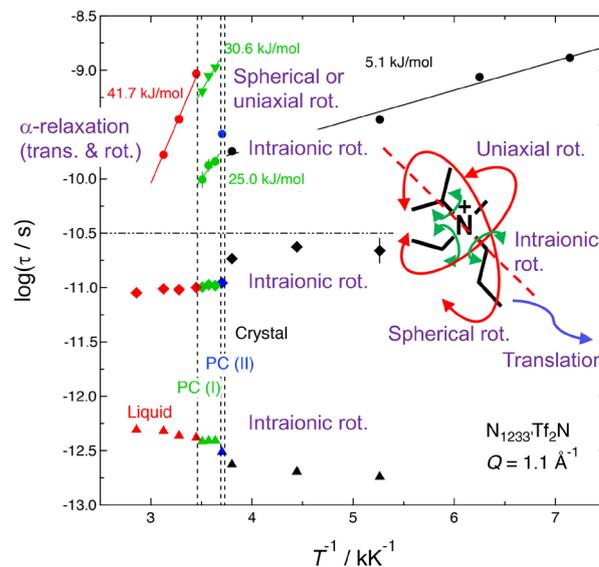


Fig. 2. Arrhenius plot of $N_{1233}$'$Tf_2N$ and assignment of each relaxation mode. The structure of $N_{1233}$' cation and possible intraionic and overall motions are schematically shown in the inset.

time range between 0.1 ps and 10 ns by means of HFBS and DCS spectrometers in NIST, USA.

As a representative result, Fig. 1 shows the QENS data for the PC1 phase of $N_{1233}$'$Tf_2N$ which were obtained at 1.1 Å$^{-1}$ and 280 K by using HFBS. The data for the PC and C phases were fitted to an elastic and two Lorentz functions, while those for the L phase to a KWW function. As shown in Fig. 1, the fittings were satisfactory for all $Q$ and $T$ data of both $N_{1223}$'$Tf_2N$ and $N_{1233}$'$Tf_2N$. Figure 2 shows the Arrhenius plot of $N_{1233}$'$Tf_2N$. In a wide time-range covering 4 orders of magnitude, there are basically 4 relaxation modes in the PC phases and 3 modes in L and C phases. Faster two modes are almost continuous over whole temperature. By analyzing the $Q$-dependence of the relaxation times and elastic incoherent structure factors (EISF), the relaxation modes were assigned as shown in Fig. 2. The faster two (for the L phase) or three (for the PC and C phases) modes are clearly of intraionic rotations. The slowest mode in the PC phases is due to the spherical and/or uniaxial rotation. The slowest mode in the L phase is the α relaxation consisting of coupled overall rotational and translational motions. A similar mode assignment was performed for $N_{1223}$'$Tf_2N$. Thus, our QENS work has clarified how the intra- and overall ionic motions are activated through the sequential phase transitions (L-PC1-PC2-C).

### References
[1] O. Yamamuro *et al.*, J. Chem. Phys. **135**, 054508 (2011).
[2] M. Kofu *et al.*, J. Phys. Chem. B **117**, 2773 (2013).
[3] F. Nemoto *et al.*, J. Phys. Chem. B **119**, 5028 (2015).
[4] M. Kofu *et al.*, J. Chem. Phys. **143**, 234502 (2015).
[5] F. Nemoto *et al.*, J. Chem. Phys., submitted.

### Authors
O. Yamamuro, M. Nirei, M. Kofu[a], M. Matsuki[b], T. Yamada[b], and M. Tyagi[c,d]
[a]J-PARC
[b]Kyushu University
[c]NIST
[d]University of Maryland

Fig. 1. The experimental QENS spectrum (closed circles) of the PC1 phase of $N_{1233}$'$Tf_2N$ obtained by HFBS. The result of the fitting, a fitted curve and each component, is also shown in the figure.

# Novel Magnetoelectric Phase in Multiferroic BiFeO$_3$

## Tokunaga Group

Simultaneous emergence of multiple "ferroic" orders, such as (anti)ferromagnetism, ferroelectricity, and ferroelasticity, brought about fruitful physics caused by non-trivial coupling among various degrees of freedom in condensed matters. Among numerous multiferroic materials, BiFeO$_3$ is perhaps the most extensively studied because of its huge spontaneous electric polarization ($P_S$) as well as high ferroelectric and antiferromagnetic ordering temperatures. Our recent careful studies of magnetoelectric effects in high-quality crystals of BiFeO$_3$ revealed existence of novel electric polarization ($P_T$) normal to the $P_S$ that can be controlled by magnetic and electric fields in a non-volatile way [1, 2]. These findings clarified that BiFeO$_3$ will be useful for non-volatile memory devices writable by electric fields, readable simply by measuring their resistance, and stable against external magnetic fields at least up to 4 T.

Emergence of $P_T$ suggests breaking of the three-fold rotational symmetry around $P_S$. Although this kind of distortion was proposed by earlier experimental studies using a synchrotron x-ray radiation facility [3], relation between magnetic order and lattice distortion has been veiled. We studied magnetostriction of a single crystal of BiFeO$_3$ with using a renewed capacitance dilatometer in pulsed magnetic fields up to 55 T (Fig. 1(a)). The results clearly resolved existence of slight (1/50,000) lattice deformation, which can be controlled by applied magnetic fields in irreversible way indicating ferroelastic nature of this material [4].

In addition to the irreversible behavior below 10 T, we observed non-monotonic change in magnetostriction between 10-15 T that suggests emergence of an intermediate phase between cycloidal and canted-antiferromagnetic phases. This feature of the intermediate phase is also observed in measurements of isothermal magnetization and electric polarization [4]. The intermediate phase grows up with increasing temperature as shown by shaded area in Fig. 1(b). According to a model calculation based on the standard Hamiltonian for this material, conical antiferromagnetic order as illustrated in Fig. 1(c) can be stabilized at a certain parameter space. Field induced transition from the cycloidal to this conical phase is expected to rotate the spin modulation
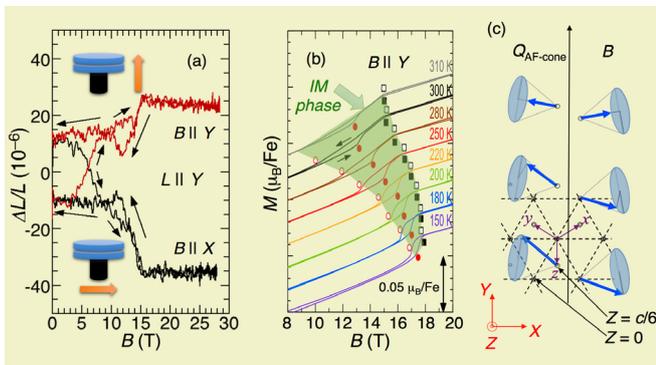
vector from $X$ to $Y$ direction in Fig. 1(c). Our neutron experiment revealed that incommensurate spin modulation along the $X$-direction in the cycloidal state becomes commensurate in the intermediate phase, which is consistent with our expectation. The magnetoelectric effects in this intermediate phase is considerably larger than those in the other phases. Our findings will open novel possibility in this well-known material.

### References
[1] M. Tokunaga *et al*., Nat. Commun. **6**, 5878 (2015).
[2] S. Kawachi *et al*., Appl. Phys. Lett. **108**, 162903 (2016).
[3] I. Sosnowska *et al*., J. Phys. Soc. Jpn. **81**, 044604 (2012).
[4] S. Kawachi *et al*., Phys. Rev. Mater. **1**, 024408 (2017).

### Authors
S. Kawachi, A. Miyake, T. Ito[a], M. Matsuda[b], W. Ratcliff II[c], S. Miyahara[d], N. Furukawa[e], and M. Tokunaga
[a]National Institute of Advanced Industrial Science and Technology (AIST)
[b]Oak Ridge National Laboratory (ORNL),
[c]NIST Center for Neutron Research, NIST,
[d]Fukuoka University,
[e]Aoyama Gakuin University

# Magnetostriction Measurements up to 190 T

## Y. Matsuda and Kobayashi Groups

Magnetic field is a unique parameter that directly acts on the spin, orbital angular momentum and phases of wavefunction of electrons in solids. High magnetic field of 100 T roughly corresponds to 100 K in energy scale. Therefore, it is expected that novel state of matter emerges under high magnetic fields, besides being just a controlling parameter of matter. Researches using non-destructive pulsed magnetic fields has been greatly successful in the last several decades both in magnet technique and measurement techniques. On the other hand, despite the fact that the ultra-high magnetic fields well above 100 T have been available using destructive pulse magnets in ISSP since 1980s, the deepening of condensed matter physics using those destructive pulse magnets is still to come. It is due to the limited space and time of the generated ultrahigh magnetic fields that is making



Fig. 1. (a) Magnetostriction of BiFeO$_3$ single crystal at 300 K measured with using the capacitance method. The insets show schematics of the capacitance cell and applied magnetic field. (b) Isothermal magnetization curves at various temperatures between 150 K and 310 K. We observed anomaly in the shaded area and assigned it as the intermediate phase. (c) Proposed spin order in the intermediate phase. This conical antiferromagnetic state can be regarded as a superposition of the cycloidal state in the *YZ* plane and the canted antiferromagnetic state within the *XY* plane.
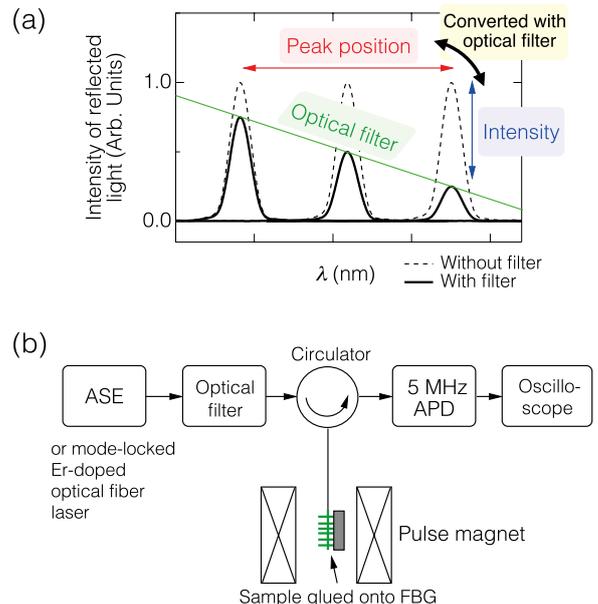


Fig. 1. (a) Schematic drawing of optical filter method for FBG peak detection (b) Schematics of developed FBG and optical filter based magnetostriction measurement system.
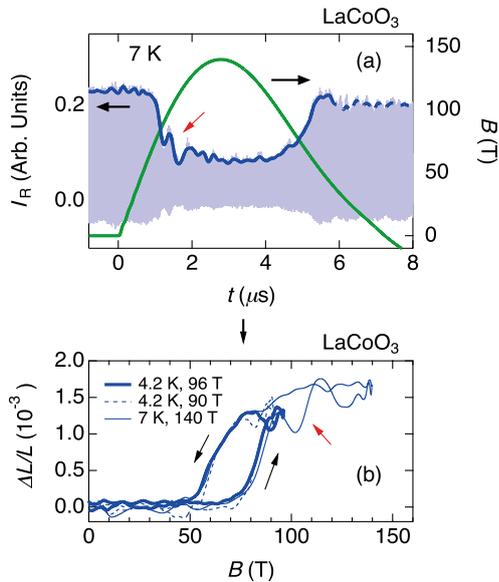
Fig. 2. (a) FBG signal from $LaCoO_3$ at 7 K up to 150 T whose pulse duration is 7 μs. (b) Magnetostriction of $LaCoO_3$ at 7 K up to 150 T obtained from the above data.

various solid state measurements difficult such as resistivity, magnetization and others.

In the present study, we report the achievement of the measurement of magnetostriction which is one of the macroscopic measure that was impossible so far under ultrahigh magnetic fields above 100 T. Developed magnetostriction measurement system relies on fiber Bragg grating (FBG) technique. FBG is an optical fiber with which one is able to detect strain of matter by observing the Bragg wavelength in the reflection. In the present study, we employed the optical filter method where the information of the shift of the Bragg wavelength is converted to the intensity of the reflected light as shown in Fig. 1(a), which can be detected at high speed of 100 MHz. The high-speed of 100 MHz is indispensable for
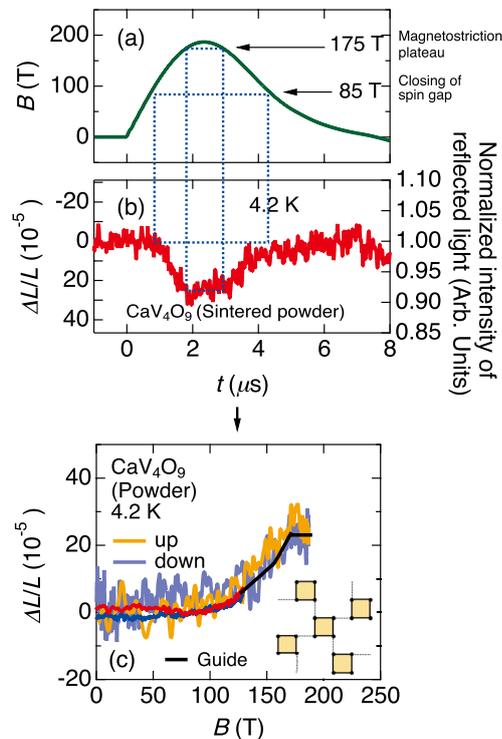


Fig. 3. (a) FBG signal from $CaV_4O_9$ at 4.2 K up to 190 T (b) Generated pulsed magnetic field using single turn coil whose pulse duration is 7 μs. (c) Magnetostriction of $CaV_4O_9$ at 4.2 K up to 190 T obtained from the above data, showing the closing of spin gap and entering into a plateau region.

the measurement under ultrahigh magnetic field generated with destructive pulse magnet because the pulse duration is only a few micron seconds. As a light source, a mode-locked Er-doped optical fiber laser is utilized as shown in Fig. 1(b). This enables one to use the modulated measurement which is more robust against noises.

We have confirmed that we are able to measure magnetostriction of $LaCoO_3$ up to 150 T as shown in Figs. 2(a) and 2(b) [1, 2], and $CaV_4O_9$ up to 190 T with the best resolution of $2.0 \times 10^{-5}$ as shown in Figs. 3(a), 3(b) abd 3(c). Using the technique with the electromagnetic flux compression technique generating magnetic field of above 500 T is under way. Also, we have applied the developed FBG based strain measurement system to non-destructive pulse magnets, where we have been successful in measuring the magnetostriction of volborthite with the resolution of $1.0 \times 10^{-6}$ [3]. The FBG based magnetostriction study under ultrahigh magnetic field for the valence fluctuation system, quantum spin system, spin-crossover systems are being carried out.

**References**
[1] A. Ikeda, T. Nomura, Y. H. Matsuda, S. Tani, Y. Kobayashi, H. Watanabe, K. Sato, Rev. Sci. Instrum. **88**, 083906 (2017).
[2] A. Ikeda, T. Nomura, Y. H. Matsuda, S. Tani, Y. Kobayashi, H. Watanabe, K. Sato, Physica B **536**, 847 (2018).
[3] A. Ikeda and Y. H. Matsuda, arXiv:1803.03404.

**Authors**
A. Ikeda and Y. H. Matsuda

# Discovery of 2D Anisotropic Dirac Cones

## I. Matsuda, Sugino, and Komori Groups

As the fifth element in the periodic table, boron atoms form numerous bulk allotropes and provide a rich chemistry and physics. Boron atomic sheets, borophene, also have an enormous number of two-dimensional (2D) polymorphs. Recently, various borophene phases have been synthesized on metal substrates, such as the $\beta_{12}$ sheet. Theoretical works have revealed numerous novel properties of these borophene phases, such as phonon-mediated superconductivity, but experimental examinations of their electronic structures are far from enough.

In the present research, we report observation of 2D anisotropic Dirac cones, Dirac delta (Δ)-cone, in $\chi_3$ borophene by the first principles calculations and angle-
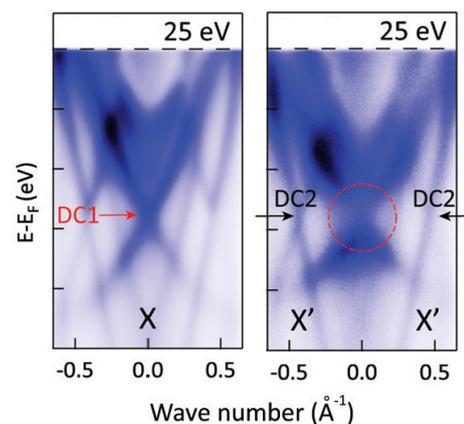


Fig. 1. Photoemission intensity plots measured with 25 eV p polarized photons at the X and X′ points. Red arrows and black arrows indicate positions of the Dirac cones of DC1 and DC2, respectively. Red broken circle show a region where one finds gap-opening for the DC1 band.
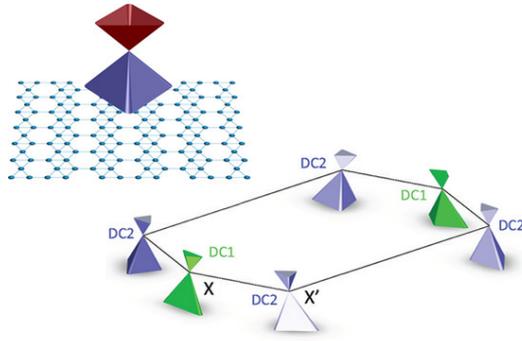
Fig. 2. Schematic drawing of the structure model of χ₃ borophene and the anisotropic Dirac cones, Δ-Dirac ones.

resolved photoemission spectroscopy measurements using synchrotron radiation. The Dirac cones are centered at the X and X′ points of the Brillouin zone, as shown in Fig.1. The calculation reveals that these Dirac cones are mainly derived from the $p_z$ orbitals of boron, with negligible contributions from the silver orbitals of the substrate. This represents that the χ₃ borophene sheet is the quasi-freestanding layer.

The atomic structure and the electronic structure of the Dirac Fermion are summarized in Fig. 2. Our results validate χ₃ borophene as the first 2D material that hosts anisotropic Dirac cones. This may stimulate further research interest and enable the realization of high-performance boron devices.

References
[1] B. Feng, J. Zhang, S. Ito, M. Arita, C. Cheng, L. Chen, K. Wu, F. Komori, O. Sugino, K. Miyamoto, T. Okuda, S. Meng, and I. Matsuda, Adv. Mater. **30**, 1704025 (2018).
[2] B. Feng, O. Sugino, R.-Y. Liu, J. Zhang, R. Yukawa, M. Kawamura, T. Iimori, H. Kim, Y. Hasegawa, H. Li, L. Chen, K. Wu, H. Kumigashira, F. Komori, T.-C. Chiang, S. Meng, and I. Matsuda, Phys. Rev. Lett. **118**, 096401 (2017).

Authors
I. Matsuda, O. Sugino, and F. Komori

# Discovery of Two-Dimensional Dirac Nodal Line Fermions in the Monolayer Cu₂Si

## I. Matsuda and Sugino Groups

Tremendous research interest has recently focused on topological semimetals which have vanishing densities of states at the Fermi level. In these materials, the valence and conduction bands can touch at either discrete points or extended lines. In the latter case, it forms nodal line semimetals. The band degeneracy points or lines are also protected by symmetries and are thus robust against external perturbations.

Two-dimensional materials have also attracted broad scientific interest because of their exotic properties and possible applications in high-speed nano-devices. Thus, realization of two-dimensional topological semimetals will
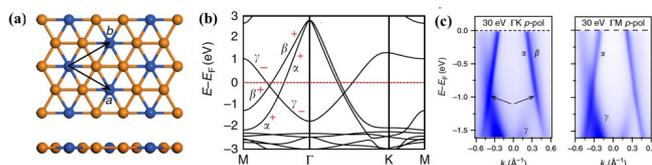


Fig. 1. (a) Atomic structure model of the monolayer Cu₂Si. (b) The calculated band dispersion curves. (c) Result of the photoemission band mapping.
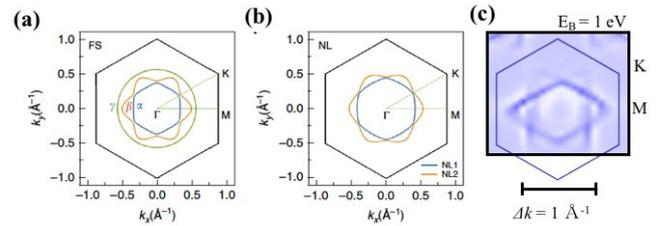


Fig. 2. (a) Fermi surface (FS), (b) nodal line (NL) of the metallic bands, α,β,γ in Fig.1. (c) Result of the photoemission band mapping for NL taken at photon energy of 30 eV and at binding energy ($E_B$) of 1 eV.

provide new platforms in academic and technological fields. In this work, we study monolayer Cu₂Si, which is composed of a honeycomb Cu lattice and a triangular Si lattice. As shown in Fig.1, all the Si and Cu atoms are coplanar and thus there is the mirror reflection symmetry with respect to the xy plane. This symmetric feature is significant for the existence of two-dimensional nodal lines. A commensurate monolayer Cu₂Si has been synthesized on a Cu (111) surface by the Si deposition. Our comprehensive theoretical calculations show the existence of two Dirac nodal loops centered around the Γ point (Fig. 1). The gapless nodal loops are protected by mirror reflection symmetry. These characteristic band structures were directly observed by angle-resolved photoemission spectroscopy measurements (Figs. 1 and 2). The theoretical and experimental results unambiguously confirm the two concentric Dirac nodal loops in monolayer Cu₂Si (Fig. 2). These results not only extend the concept of Dirac nodal lines from three- to two-dimensional materials, but also provide a new platform to realize novel devices at the nanoscale.

Reference
[1] B. Feng, B. Fu, S. Kasamatsu, S. Ito, P. Cheng, C.-C. Liu, S. K. Mahatha, P. Sheverdyaeva, P. Moras, M. Arita, O. Sugino, T.-C. Chiang, K. Wu, L. Chen, Y. Yao, and I. Matsuda, Nature Comm. **8**, 1007 (2017).

Authors
I. Matsuda and O. Sugino

# Determination of Element-Specific Complex Permittivity with Soft X-Ray Segmented Cross Undulator at SPring-8 BL07LSU

## I. Matsuda, Akai, Wadati, Harada, and Shin Groups

Permittivity (or conductivity) is a quantity that characterizes a response of a matter by an electric field, such as an electromagnetic wave. It has historically been used to develop varieties of electronic and optical devices that have supported our society today. Determinations and understandings of permittivity of matters have been one of the highest priority tasks of science and technology. Recently, the requirement has reached to the ultraviolet (UV) ~soft X-ray (SX) region due to necessity of developing the extended-UV (EUV) lithography for the advanced technologies or ultra-high-resolution SX experiments for the frontier sciences, for examples.

A permittivity has been often approximated as a (dielectric) constant but it is essentially the tensor quantity that is composed of diagonal and off-diagonal components. The diagonal and the off-diagonal element carries non-magnetic
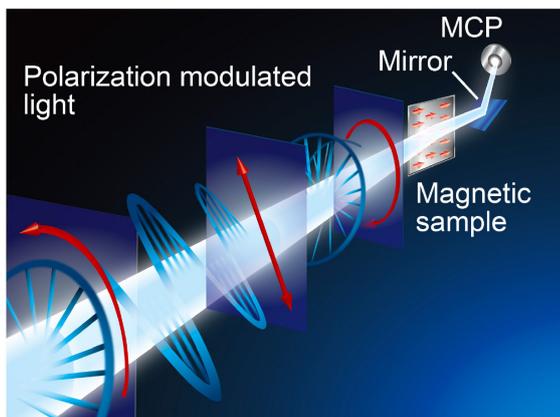
Fig. 1. Image of the polarization modulated light with the L-MOKE set up at SPring-8 BL07LSU.

and magnetic information of a matter, respectively, and it is the latter that has been significant to understand the spin polarization or the magnetization. The individual elements are complex, being composed of the real and imaginary parts. The determination has been widely made by a probing light with the polarization modulation (frequency of p) and the measurement of the sample optical responses at the two frequencies (p, 2p). Such an experiment is easily achieved by transmitting the incident light through crystals that allow electric or mechanic controls of the polarization. Nowadays, one can find varieties of commercial polarization modulators for visible light and hard X-ray but for the EUV SX region. This is mainly because the light absorbance in a matter in this region is so large that it does not allow the transmission and the light can only survive in vacuum due to absorption by air molecules. In addition, the 'abnormal' optical response at the absorption edges of the composing element has also intervened the precise evaluation. Up to now, the determination has been made only with a help of simulations based on the atomic parameters and the indirect experimental data,
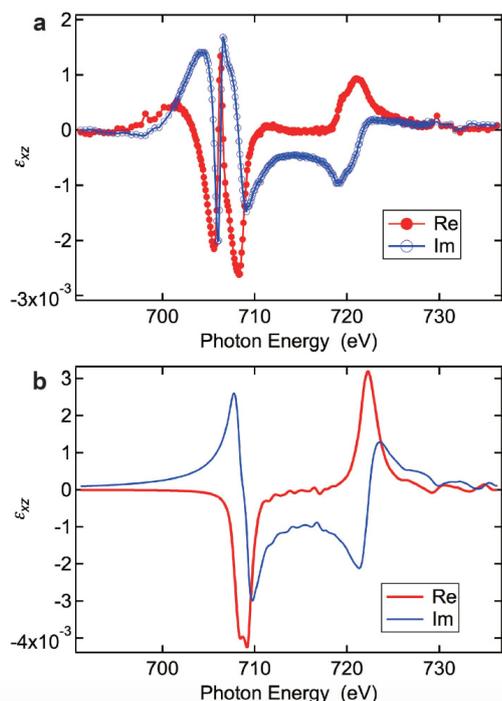
which has often left the large uncertainty in the permittivity values. Thus, the estimation has been made for systems that are simple and not for the complicated or non-uniform ones. To overcome these difficulties, one can use synchrotron radiation, generated by electrons that already exist in vacuum and one can control the polarization by the electron trajectory that is regulated by the external magnetic field.

Here, we developed a novel SX source of the segmented cross undulator that can make the continuous polarization modulation (p) of the light and carried out the magneto-optical measurement (p, 2p) of the buried Fe nanolm at the Fe L-edge absorption edge in SX region (Fig. 1). As shown in Fig. 2, we succeeded in directly determining the complex permittivity and we found that the first-principles calculation with the Korringa-Kohn-Rostoker (KKR) formalism gave the perfectly matching results. It is of note that a spectral dip/ peak at 705 eV in experiment is due to the optical response by the film structure that has not been taken into account in the calculation. Our procedure determines the permittivity of a sample in UV~SX region with high precisions, which is significant for the better understanding of the light-matter interaction. It also opens new technical examination method to seek for the best materials for optical elements, for examples, in the EUV lithography technology or in the laser technology of high harmonic generation lasers, high-brilliant synchrotron radiation, and X-ray free electron laser.

**References**
[1] S. Yamamoto, Y. Senba, T. Tanaka, H. Ohashi, T. Hirono, H. Kimura, M. Fujisawa, J. Miyawaki, A. Harasawa, T. Seike, S. Takahashi, N. Nariyama, T. Matsushita, M. Takeuchi, T. Ohata, Y. Furukawa, K. Takeshita, S. Goto, Y. Harada, S. Shin, H. Kitamura, A. Kakizaki, M. Oshima, and I. Matsuda, J. Syn. Rad. **21**, 352 (2014).
[2] I. Matsuda, A. Kuroda, J. Miyawaki, Y. Kosegawa, S. Yamamoto, T. Seike, T. Bizen, Y. Harada, T. Tanaka, and H. Kitamura, Nucl. Instrum. Methods Phys., Sect. A **767**, 296 (2014).
[3] Y. Kubota, Sh. Yamamoto, T. Someya, Y. Hirata, K. Takubo, M. Araki, M. Fujisawa, K. Yamamoto, Y. Yokoyama, M. Taguchi, S. Yamamoto, M. Tsunoda, H. Wadati, S. Shin, and I. Matsuda, J. Elec. Spec. Rel. Phenom. **220**, 17 (2017).
[4] Y. Kubota, M. Taguchi, Sh. Yamamoto, T. Someya, Y. Hirata, K. Takubo, M. Araki, M. Fujisawa, H. Narita, K. Yamamoto, Y. Yokoyama, S. Yamamoto, M. Tsunoda, H. Wadati, S. Shin, and I. Matsuda, Phys. Rev. B **96**, 134432 (2017).
[5] Y. Kubota, Y. Hirata, J. Miyawaki, S. Yamamoto, H. Akai, R. Hobara, Sh. Yamamoto, K. Yamamoto, T. Someya, K. Takubo, Y. Yokoyama, M. Araki, M. Taguchi, Y. Harada, H. Wadati, M. Tsunoda, R. Kinjo, A. Kagamihata, T. Seike, M. Takeuchi, T. Tanaka, S. Shin, and I. Matsuda, Phys. Rev. B **96**, 214417 (2017).

**Authors**
Y. Kubota, Y. Hirata, J. Miyawaki, S. Yamamoto, H. Akai, M. Araki, Y. Harada, H. Wadati, S. Shin, and I. Matsuda

Fig. 2. a. $\varepsilon_{xz}$ spectra of the Fe nanofilm at the L-edge obtained by the L-MOKE measurement with the polarization modulated light. Red lled circles and blue open circles represent its real and imaginary parts, respectively. b. $\varepsilon_{xz}$ spectra of bulk Fe (bcc) at the L-edge obtained by the first-principles calculation with the KKR formalism. Red and blue lines represent its real and imaginary parts, respectively.

# Interface Hydrogen Bonds at the HeteroJunction between Proton-Donating and Proton-Accepting Self-Assembled Monolayers

## I. Matsuda, Mori, amd Yoshinobu Groups

Hydrogen bondings have been significant in chemical and biological systems. It has been known to fix molecular configurations and it is also flexible for breaking and making bonds between molecules at room temperature. Additionally, a hydrogen bond also effectively assists the proton ($H^+$) transfer between the donor and the acceptor sites along the bond. The transfer of one whole $H^+$ ion substantially changes charge distributions between the molecules. Based
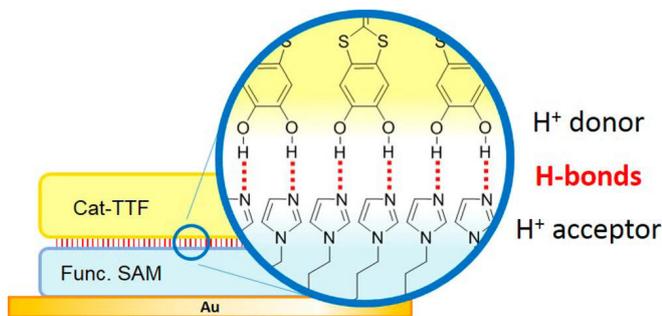
Fig. 1. Schematic drawing of hydrogen bonds at the interface between Cat-TTF and functional SAM (Im-SAM) on Au(111).

on this electron-proton concerting effect, highly conductive pure organic molecular crystals have been realized at the partially deprotonated molecular crystals of catechol-fused ethylenedithiotetrathiafulvalene ($H_2$Cat-EDT-TTF). These facts motivate us to design a possible control of the film conductivity depending of the proton position between $H^+$ donor and acceptor layers, which leads to a new concept for driving electronic device. As the first step of this ambitious goal, we created a hydrogen-bonding heterogeneous interface consisting of a bilayer of the $H^+$-donating and –accepting molecules on a substrate (Fig. 1).

For the $H^+$-acceptor molecular layer, we adopted an imidazole-terminated alkanethiolate self-assembled monolayer (Im-SAM) prepared on the Au(111) substrate. The imidazole molecule can accept $H^+$ at the imino N site and stabilize it as an imidazolium cation. At the saturation coverage of alkanethiolate-based SAMs, the molecules are in a closely packed standing-up form and the end group tends toward the open side on the SAM. The molecular orbitals and chemical properties of the functional end groups are hardly perturbed from Au substrates due to the sufficient thickness of the closely packed alkylene chains in the SAMs. Thus, the imino N atom on Im-SAMs is expected to make hydrogen bonds as $H^+$ acceptor sites with $H^+$-donating molecules.

For the counterpart, the $H^+$-donor molecular layer, we focused on the adsorption of the catechol-fused bis(methylthio)tetrathiafulvalene ($H_2$Cat-BMT-TTF) molecules on the Im-SAM film. The hydroxyl groups at the catechol moiety in $H_2$Cat-BMT-TTF should act as the $H^+$-donating group, by analogy to the conductive $H_2$Cat-EDT-TTF complexes, in

which it has been elucidated that the TTF moiety is electron-donating and the hydroxyl groups in the catechol moiety accept the electron by pushing out $H^+$.

We confirm the formation of a hydrogen-bonding heterogeneous bilayer that consists of the $H_2$Cat-BMT-TTF layer and the Im-SAM film, systematically elucidated by AFM, X-ray photoelectron spectroscopy, infrared absorption spectroscopy, and density functional theory calculations. Figure 2 shows one of the evidence showing clear infrared spectral signals of the bilayer system. The broad feature at frequency of 2500-3500$cm^{-1}$ indicates strong hydrogen bonds at the heterointerface. These results provide new insight for designing electron-proton functions in adsorption systems.

**Reference**
[1] H. S. Kato, S. Yoshimoto, A. Ueda, S. Yamamoto, Y. Kanematsu, M. Tachikawa, H. Mori, J. Yoshinobu, and I. Matsuda, Langmuir **34**, 2189 (2018).

**Authors**
H. S. Kato, H. Mori, J. Yoshinobu, and I. Matsuda

# Observation of Second Harmonic Generation in Soft X-Ray and Study of its Element Selectivity

## I. Matsuda, Akai, Wadati, and Shin Groups

Second harmonic generation (SHG) is the well-known nonlinear optical frequency conversion and it has been a significant probe to investigate the electronic properties of matter. In the SHG process, optical fields interact with a medium of broken inversion symmetry, resulting in production of a double field frequency. Recent development of a free electron laser (FEL), the high brilliant laser in the energy range from vacuum ultraviolet to X-ray, allows to explore nonlinear optical effects in these energy ranges. All of the earlier studies on non-linear optics in those energy ranges reported experiments conducted under a transmission geometry in order to acquiring enough signals by meeting phase-matching condition. In the soft X-ray range, the reflection geometry is preferred because the light in the energy range is strongly absorbed by materials. However, in the reflection geometry, the non-linear optical experiments suffer the extremely low signals due to the absence of coherent amplification caused by the phase matching.

Here, we demonstrate observation of SHG from a non-centrosymmetric crystal by employing the resonance effect described below, even under the reflection geometry (Fig. 1). The experiment was carried out by using a soft
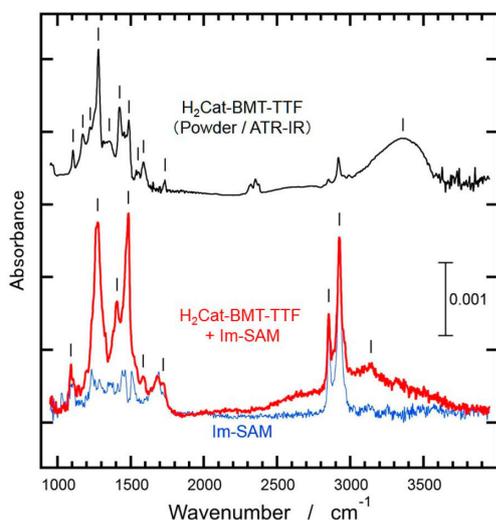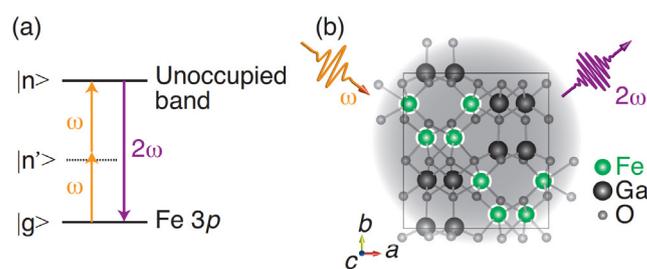


Fig. 2. Infrared (IR) reflection absorption spectra for $H_2$Cat-BMT-TTF adsorbed on Im-SAM (red) and for Im-SAM (blue), in comparisons with the IR spectrum for the $H_2$Cat-BMT-TTF powder (black).



Fig. 1. Second harmonic generation in the GaFeO$_3$ crystal using Fe 3p resonance. (a) Energy diagram of SHG. The notations, g, n', and n represent the ground state, virtual state, and excited state, respectively. (b) Projection view along the c axis of the crystal structure of GaFeO$_3$.
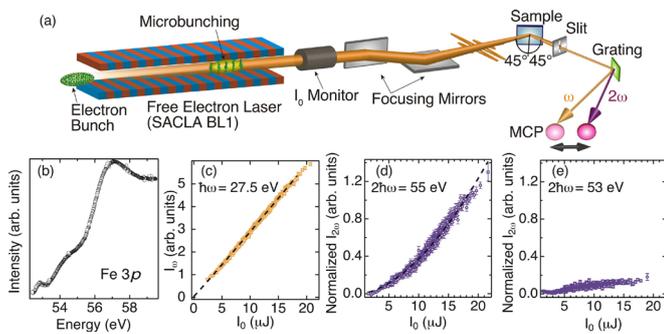
Fig. 2. (a) Schematic diagram of the SXFEL beamline at SACLA and the SHG measurement system. (b) Fe 3p absorption spectrum of the GaFeO3 crystal. (c) Intensity plot of the ω component of the reflected SXFEL pulses, $I_\omega$, with respect to the correspondent incident intensity, $I_0$, at the photon energy $\hbar\omega = 27.5$ eV. (d) Plot of $I_{2\omega}$ at the photon energy of $2\hbar\omega = 55$ eV. (e) Plot of $I_{2\omega}$ at the photon energy of $2\hbar\omega = 53$ eV. The dashed lines shown in (c) and (d) were fitted by a power law.

X-ray FEL (SXFEL) at SACLA in Harima. SHG signals were detected when the photon energy with double frequency 2ω was above the absorption edge of the sample, as shown in Fig. 2. The metal M-edge resonance inherently indicates addition of element specificity to the SHG experiment. Moreover, the reflection measurement geometry indicates that the present method can be used for various samples and experimental conditions. The optical frequency conversion with SXFEL is expected to selectively probe the electronic properties of nonlinear bulk crystals and the interfaces in heterostructures that are composed of multi-element materials.

### Reference
[1] Sh. Yamamoto, T. Omi, H. Akai, Y. Kubota, Y. Takahashi, Y. Suzuki, Y. Hirata, K. Yamamoto, R. Yukawa, K Horiba, H. Yumoto, T. Koyama, H. Ohashi, S. Owada, K. Tono, M. Yabashi, E. Shigemasa, S. Yamamoto, M. Kotsugi, H. Wadati, H. Kumigashira, T. Arima, S. Shin, and I. Matsuda, Phys. Rev. Lett. **120**, 223902 (2018).

### Authors
Sh. Yamamoto, Y. Hirata, S. Yamamoto, H. Wadati, S. Shin, and I. Matsuda

# Dzyaloshinskii-Moriya Interaction in α-Fe2O3 Measured by Magnetic Circular Dichroism in Resonant Inelastic Soft X-ray Scattering

## Harada Group

Dzyaloshinskii-Moriya interaction (DMI) is an asymmetric exchange interaction induced by a lack of inversion symmetry in materials through spin-orbit coupling. Even though DMI is much weaker than the Heisenberg exchange interaction, DMI plays an essentially important role to determine magnetism and related physical properties in various systems. DMI is expressed by the formula $D_{ij} \cdot S_i \times S_j$, but the direction and magnitude of $D_{ij}$ has been difficult to determine both theoretically and experimentally. Among new approaches explored to measure DMI, selective observation of the electronic structure that is responsible for the DMI is of crucial importance. α-Fe2O3 is a prototype material of DMI and shows weak ferromagnetism due to the DMI at room temperature. However, even for α-Fe2O3, the electronic structure leading to its weak ferromagnetism

has not been experimentally identified. Thus, we measured magnetic circular dichroism (MCD) in resonant inelastic soft x-ray scattering (SX-RIXS) of α-Fe2O3 [1]. RIXS-MCD enables us to probe the MCD for each dd excitation, which is very sensitive to the symmetry of the d orbitals, and is expected to give an insight into the origin of the weak ferromagnetism induced by DMI in α-Fe2O3.

The x-ray absorption spectra (XAS) and RIXS experiments of an α-Fe2O3 single crystal were conducted at the HORNET end-station at BL07LSU in SPring-8. MCD in XAS and RIXS was measured by using a compact magnetic circuit with permanent Nd-Fe-B magnets [2]. Figure 1(a) compares the experimental and calculated results of XAS of α-Fe2O3. Peak splittings (Nos. 1 and 2) attributed to the crystal field effect and a satellite feature at $h\nu \approx 713.25$ eV assigned to a charge-transfer state were clearly observed. No discernible XAS-MCD signal was detected. XAS is well reproduced by *ab initio* charge-transfer multiplet calculation. Figures 1(b) and 1(c) show RIXS-MCD spectra measured by two different experimental configurations. In the configuration of $k_{in} \parallel \langle 11\bar{2} \rangle$ (Fig. 1(b)), the magnitude of RIXS-MCD was relatively small at any excitation energies employed compared with that in the configuration of $k_{in} \parallel \langle 1\bar{1}0 \rangle$ (Fig. 1(c)), where the dd excitation at 1.8 eV (peak B) showed RIXS-MCD for $h\nu > 713.25$ eV (No. 3, the charge-transfer satellite), while no RIXS-MCD was observed by the excitation of the main absorption peaks (Nos. 1 and 2). Thus, RIXS-MCD showed the crystal orientation and excitation energy dependences. The observed RIXS-MCD is qualitatively well described by the calculations (Fig. 1(d)). RIXS-MCD in peak B′ is almost absent for the excitations around the main peaks of the $L_3$ edge (Nos. 1′ and 2′), while small but clear RIXS-MCD is found at peak B′ for the excitations above the satellite structure (No. 3′). The more detailed configuration analysis has revealed that the RIXS-MCD derives from spin flip excitations at delocalized $e_g$ orbitals. By the combination of the experiments and calcu-
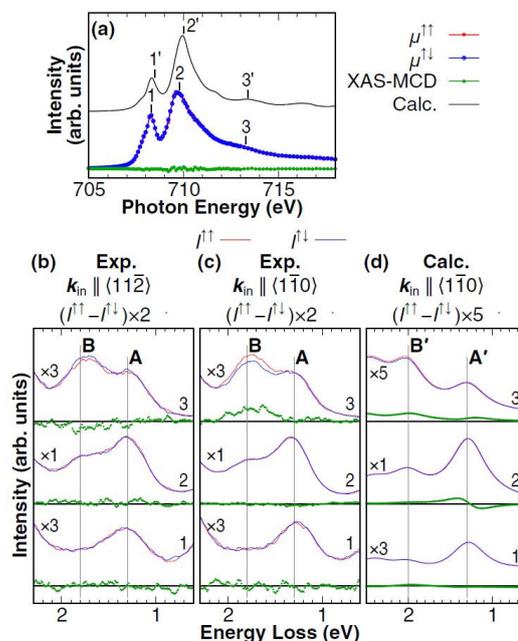


Fig. 1. Experimental and calculated results of Fe $L_3$-edge XAS- and RIXS-MCD spectra of α-Fe2O3. (a) Experimental and calculated Fe $L_3$-edge XAS spectra. (b) and (c) Experimental RIXS-MCD spectra in the configurations of $k_{in} \parallel \langle 11\bar{2} \rangle$ and $k_{in} \parallel \langle 1\bar{1}0 \rangle$. (d) Calculated RIXS-MCD spectra in the configuration of $k_{in} \parallel \langle 1\bar{1}0 \rangle$. The red ($I^{\uparrow\uparrow}$) and blue ($I^{\uparrow\downarrow}$) spectra represent the intensity of the scattered x ray for the spin polarization of the incident x ray parallel and antiparallel to the direction of the sample magnetization, respectively. The numbers in (b,c,d) indicate the excitation energies shown in (a).

lations, RIXS-MCD has unraveled that the origin of DMI in $\alpha$-$Fe_2O_3$ is the $e_g$ orbitals, which are strongly hybridized with the $2p$ orbitals of oxygen atoms.

The results demonstrate the important capability of RIXS-MCD to sensitively extract the magnetic information from MCD of each $dd$ excitation in the weak-ferromagnet, where the net magnetic moments are so small that XAS-MCD is not applicable. With this advantage, RIXS-MCD is expected to be more widely applied to the weak ferromagnetism and spin spiral induced by DMI. Furthermore, bulk sensitivity and element selectivity of RIXS will also promote the measurement of RIXS-MCD, and thus RIXS-MCD could be a promising technique to obtain the information about the ground-state spin state. Finally, it is worth mentioning that the computational calculations have now become powerful enough to discuss the very small magnitude of RIXS-MCD for the realistic low-symmetry system, and will advance the more precise analysis of the experimental results and give more complete comprehension of physical properties.

**References**
[1] J. Miyawaki, S. Suga, H. Fujiwara, M. Urasaki, H. Ikeno, H. Niwa, H. Kiuchi, and Y. Harada, Phys. Rev. B **96**, 214420 (2017).
[2] J. Miyawaki, S. Suga, H. Fujiwara, H. Niwa, H. Kiuchi, and Y. Harada, J. Synchrotron Rad. **24**, 449 (2017).

**Authors**
J. Miyawaki, S. Suga[a], H. Fujiwara[a], M. Urasaki[b], H. Ikeno[b], H. Niwa, H. Kiuchi, and Y Harada
[a]Osaka University
[b]Osaka Prefecture University

# Enhancement of the Hydrogen-Bonding Network of Water Confined in a Polyelectrolyte Brush

## Harada Group

In the crowded environment of a living cell, several biomolecular polyelectrolytes−especially proteins, nucleic acids, and complex sugars−are compressed together. Water encapsulated between the aforementioned entities is no longer a simple space-filling medium but is believed to exhibit intriguing hydrogen-bonding networks depending on its molecular dimensions and interfacial properties. This unique hydrogen-bonding structure of water in the vicinity of polyelectrolytes should significantly affect the specific structure and functions of biomolecules and their assemblies. Hence, it is imperative to devise a novel method for investigating the local hydrogen-bonding structure of water near polyelectrolytes, which can aid in the understanding of the functions of biological systems. A polyelectrolyte brush, a surface-tethered polymer layer is a proper model interface of polymeric soft materials, such as proteins. A recent study using microscopic infrared (IR) spectroscopy indicated that water molecules are confined in a polyelectrolyte brush with a highly ordered hydrogen-bonding network. The formation of a hydration layer of polyelectrolytes and the resulting hydrogen-bonding network is expected to be crucial to controlling the properties of biomolecules, such as lubrication and antifouling. This study sheds light on the local hydrogen-bonding structure of water confined in a charged polyelectrolyte brush and reveals that the hydrogen-bonding structure of water confined in the polyelectrolyte brush is
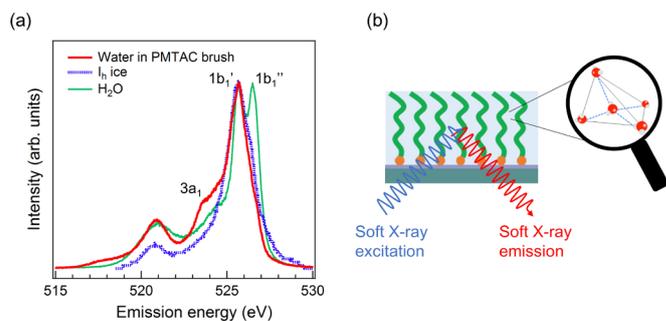


Fig. 1. (a) O 1s soft X-ray emission spectra of water confined in the polyelectrolyte brush, the dry brush measured in vacuum, liquid $H_2O$, and ice $I_h$. The excitation energy is 550.3 eV, which is well above the ionization threshold. (b) Schematic of the hydrogen-bonding structure of water confined in the PMTAC brush.

very similar to ice $I_h$, even at room temperature [1].

O 1s X-ray emission spectroscopy (XES) experiments of water confined in the polyelectrolyte brush were performed at the SPring-8 synchrotron radiation facility using the BL07LSU HORNET station. Figure 1(a) compares the O 1s XES spectra of the water confined in the poly[2-(methacryloyloxy)- ethyltrimethylammonium chloride] (PMTAC) brush, bulk liquid water, and ice $I_h$. The XES spectra of the bulk liquid water and ice $I_h$ are shown with the same $1b_1$ peak intensity as that of confined water to compare the spectral shape. The XES spectra of the confined water and ice $I_h$ are very similar; the $1b_1''$ peak, which is observed in the spectrum of bulk liquid water, is negligible. The similarity between the two XES spectra is quite surprising as a significant enhancement of hydrogen-bonding is observed even at room temperature in the water confined in the PMTAC brush. Moreover, enhanced spectral intensity is observed around the $3a_1$ region for the confined water as compared to that in ice $I_h$ and bulk liquid water. The $3a_1$ peak, which is attributed to the dipole-forbidden transition ($3a_1 \rightarrow 1a_1$) in tetrahedral symmetry, is not observed for ice $I_h$ and is smeared out in the case of bulk liquid water because of the high sensitivity of the $3a_1$ orbital to the distribution of the hydrogen-bond strength. Therefore, the enhancement of the $3a_1$ peak observed for the confined water can be explained by the fact that the hydrogen bonds are distorted (not straight O−H···O bonds), albeit somewhat ordered, in the PMTAC brush.

Our XES results confirm that these techniques are extremely sensitive to the presence/absence and distortion of hydrogen-bonding. A majority of water molecules in the polyelectrolyte brush are held together by one type of hydrogen-bonding configuration: possibly a slightly distorted but ordered hydrogen-bonding configuration even at room temperature. The distorted picture is only a speculation from the emergence of the $3a_1$ state and the consideration of the possible hydrogen-bond structure in the vicinity of the charged site, which needs further study from both experimental and theoretical aspects. We believe that XES will pave the way for novel, important research fields in the near future.

**Reference**
[1] K. Yamazoe, Y. Higaki, Y. Inutsuka, J. Miyawaki, Y. −T. Cui, A. Takahara, and Y. Harada, Langmuir **33**, 3954 (2017).

**Authors**
K. Yamazoe, Y. Higaki[a], Y. Inutsuka[a], J. Miyawaki, Y. −T. Cui, A. Takahara[a], and Y. Harada
[a]Kyusyu University

# Capturing Ultrafast Magnetic Dynamics by Time-Resolved Soft X-Ray Magnetic Circular Dichroism

## Wadati, I. Matsuda, and Shin Groups

Control of electron, magnetic, and lattice states by optical excitations in magnetically ordered materials has attracted considerable attention due to their potential applications in electronic and magnetic recording media functioning on an ultrafast time scale below nanosecond (ns, $10^{-9}$ second, GHz range). To capture their non-equilibrium dynamics, ultrafast time-resolved experiments have been carried out using a bunched synchrotron light source, and x-ray free electron lasers [1]. FePt thin films have drawn intense research interest owing to their potential for high density recording applications by using their magnetism. Recently, Lambert *et al*. have showed that circularly polarized laser pulses can induce a small helicity-dependent magnetization in FePtAgC granular film [2]. This finding suggests the possibility of all-optical switching of the magnetism in FePt having very short recording-time windows on the ps time scale.

Here, we present a setting for time-resolved (Tr-) x-ray absorption spectroscopy (XAS) and Tr- x-ray magneto circular dichroism (XMCD) in the partial electron yield (PEY) and total fluorescence yield (TFY) modes to measure non-transmissive as-grown samples at nearly normal incidence [3]. The results of Tr-XMCD experiments for as-grown FePt films with non-transmissive substrates are reported. A photo-induced ultrafast demagnetization at the Fe sites of the FePt thin film are observed within the experimental time resolution of 50 ps for Tr-XMCD at SPring-8.

Figure 1 shows an overview of the experimental setup for Tr-XAS, Tr-XMCD, and Tr- resonant soft x-ray scattering (RSXS) measurements in the soft x-ray region at BL07LSU of SPring-8. Tr-RSXS is performed at the $\theta < 90°$ side of the experimental chamber. The scattering is detected by the micro-channel plate (MCP) or avalanche photodiode (APD) installed on the $2\theta$ motion of the diffractometer. On the other hand, XAS and XMCD in the PEY or TFY modes are measured at the $\theta > 90°$ side of the chamber. Emitted photo-electrons or x-ray fluorescence are caught by another MCP topped on the linear motion. The femtosecond Ti:sapphire laser with a wavelength of 800 nm is introduced into the XAS and RSXS chamber. The laser irradiates samples and photo-induced dynamics of the electronic and structural evolutions are examined by means of a pump-probed technique. The laser pulses with 1 kHz repetition rate are synchronized with selected bunches of the synchrotron and delayed electronically. The signals of the MCP or APD are amplified and gated on the oscilloscope or Boxcar integrator which is triggered by the laser pulses (Fig. 1 (b)).
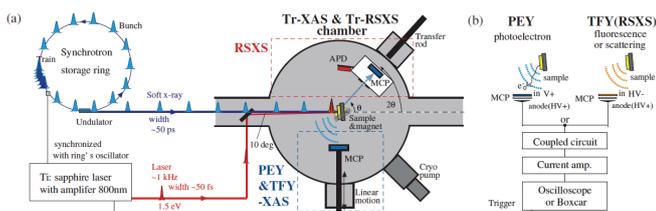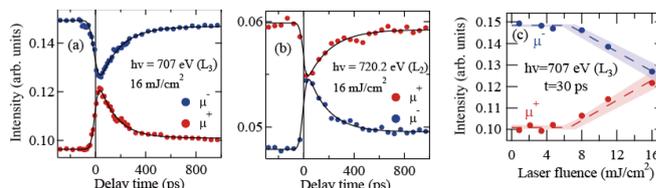


Fig. 2. (a) Time-evolutions of XMCD taken in the PEY mode at(a) $L_3$ (h$\nu$=707.0 eV) and (b) $L_2$ (h$\nu$=720.2 eV) edges for the FePt thin film at room temperature. (c) Laser-fluence dependence of Tr-XMCD intensities ($\mu$+ and $\mu$−) at t=30 ps on the $L_3$ edge (h$\nu$=707.0 eV). The dashed lines denote results of the linear fittings having a threshold.

The time evolutions of the FePt thin film with 16 mJ/cm$^2$ laser irradiations are given in Fig. 2 (a) at h$\nu$=707.0 eV ($L_3$ edge) and (b) at 720.2 eV ($L_2$ edge), respectively. As can be seen, almost similar time-evolutions are observed for the Fe $L_{2,3}$ edges. XMCD exhibits a reduction in its intensity by ~90% of the original value ~30 ps after the pump pulse. Then the XMCD exhibits a slow recovery of the magnetization with a time constant of ~150 ps. In addition, the magnetization is not recovered to the original value even at t=1500 ps, which is completed before the next bunch arrives after ~342 ns. Figure 2 (c) gives the Tr-XMCD intensities at t = 30 ps as a function of the laser fluence. Threshold-like behavior is observed at 6.5 mJ/cm$^2$ for t = 30 ps, which is estimated by the linear fittings for the fluence dependences. These results indicate that the photoinduced effect will not be a simple thermal effect.

The less-distorted PEY method presented in this study will provide an opportunity for applying a sum rule analysis to XMCD spectra in the ultrafast pump-probed spectroscopy for various magnetic materials, which would be very useful to explore the all-optical switching in spintronics devices such as FePt, Co/Pt multi-layers and so forth. On the other hand, the bulk sensitive TFY method will allow us to measure the dynamics of bulk samples showing various quantum phenomena.

### References
[1] A. Kirilyuk, A. V. Kimel, and T. Rasing, Rev. Mod. Phys. **82**, 2731 (2010) and reference there in.
[2] C.-H. Lambert, S. Mangin, B. S. D. Ch. S. Varaprasad, Y. K. Takahashi, M. Hehn, M. Cinchetti, G. Malinowski, K. Hono, Y. Fainman, M. Aeschlimann, and E. E. Fullerton, Science **345**, 1337 (2014).
[3] K. Takubo, K. Yamamoto, Y. Hirata, Y. Yokoyama, Y. Kubota, S. Yamamoto, S. Yamamoto, I, Matsuda, S. Shin, T. Seki, K. Takanashi, and H. Wadati, Appl. Phys. Lett. **110**, 162401 (2017).

### Authors
K. Takubo, K. Yamamoto, Y. Hirata, Y. Yokoyama, Y. Kubota, S. Yamamoto, S. Yamamoto, I. Matsuda, S. Shin, T. Seki[a], K. Takanashi[a], and H. Wadati
[a]Institute for Materials Research, Tohoku University

Fig. 1. (a) Overview of the setup for Tr-XAS and Tr-RSXS measurements at BL07LSU of SPring-8. The Ti-sapphire laser with a ~1 kHz repetition rate, which is synchronized with the bunches of the synchrotron, is introduced into the experimental chamber. (b) Electrical circuits for the detectors.